J. Fluid Mech. (2010), *vol.* 656, *pp.* 260–297. © Cambridge University Press 2010
doi:10.1017/S0022112010001114

A weakly nonlinear evolution model for long internal waves in a large lake

TAKAHIRO SAKAI† AND L. G. REDEKOPP
Department of Aerospace & Mechanical Engineering, University of Southern California,
Los Angeles, CA 90089-1191, USA

(Received 11 February 2009; revised 26 February 2010; accepted 28 February 2010;
first published online 26 May 2010)

A wind-forced weakly nonlinear weakly dispersive evolution model is derived for a continuously stratified circular lake of slowly varying depth under the effect of the Earth's rotation. The model was numerically integrated to investigate the evolution of long internal waves of vertical mode one for various sets of environmental parameters. It is demonstrated that the Kelvin wave steepens as it propagates, and the steepened front subsequently generates a train of oscillatory waves. It is demonstrated that Poincaré waves do not steepen, but their amplitude is modulated in an oscillatory manner with time, exhibiting a pseudo recurrence character. The model was applied to the wind forced problem, confirming that Kelvin and Poincaré waves are the dominant response. Energy partition among Kelvin and Poincaré wave modes is estimated as a function of wind-forcing parameters. For large lakes, the most significant wave amplitude is found in the Kelvin wave mode, but the gross field energy is most significantly contained in Poincaré wave modes.

1. Introduction

The hydrodynamics of a lake is to a greater or lesser extent affected by Coriolis acceleration introduced by the Earth's rotation, and Coriolis acceleration has a determining role in lake motions when the horizontal scale is sufficiently large. A useful measure of this scale is the Rossby radius $R_0 = c_s/f$, where c_s is a characteristic velocity scale and f is the inertial frequency. Since typical characteristic phase speeds of internal waves are smaller than that of surface waves by a few orders of magnitude, the effect of Earth's rotation, as well as the amplitude of fluid motion, are significantly greater in the case of internal waves as opposed to barotropic motions (Csanady 1975). As a rule of thumb, if the width of a lake is greater than the Rossby radius, the effect of the Earth's rotation needs to be taken into account. In such a large lake, a typical response excited by wind stress forcing over the lake surface is dominated by Kelvin and Poincaré waves of vertical mode one. A Kelvin wave is a shore-trapped wave having a large alongshore current, and the amplitude decays exponentially away from the shore. It propagates in a cyclonic direction along the shore with frequency less than the inertial frequency. A Poincaré wave is an offshore type of wave having its largest perturbation current located near the basin centre, rotating anti-cyclonically with frequency larger than the inertial frequency.

The theoretical foundations based on the linear hydrostatic assumption applied to the hydrodynamic equations of motion were developed by Lamb (1932) and Csanady (1967) for a circular lake of uniform depth. One of the beautiful results

---

† Email address for correspondence: tsakai@usc.edu

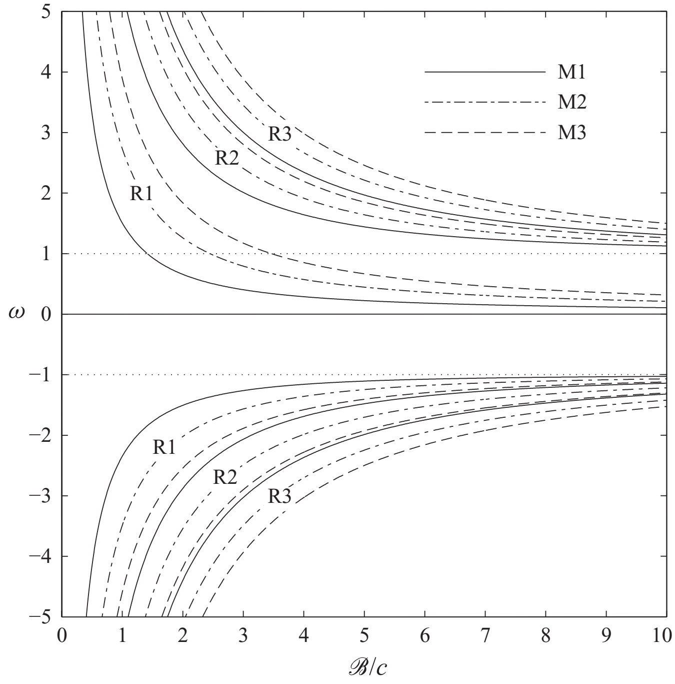

FIGURE 1. Eigenfrequency ω as a function of scaled Burger number $\mathscr{B}/c$ for the lowest three azimuthal (M) and radial (R) modes. In the northern hemisphere the positive (+) and negative (−) frequencies represent the waves of cyclonic (counter-clockwise) rotation and of anti-cyclonic (clockwise) rotation, respectively.

in this theory is a dispersion relation as shown in figure 1, providing a discrete horizontal modal frequency space, with either cyclonic or anti-cyclonic polarity. The dimensionless frequency ω/f is exhibited as a function of the Earth's rotation, which is parameterized as a ratio between the lake radius r_0 relative to the Rossby radius R_0 (i.e. the Burger number $\mathscr{B}$). Since the phase speed of internal waves is dependent on the stratification, which is in general seasonally varying, the effect of the Earth's rotation also varies seasonally (Antenucci, Imberger & Saggio 2000).

Real lakes are confined within complex boundaries, and they are subject to temporally and spatially irregular forcing, resulting in a 'zoo' of complex responses comprising internal waves, topographic gyres and coastal jets (Csanady 1975). To predict such physical responses, three-dimensional hydrodynamic models have been developed and their use has expanded in recent years (e.g. Beletsky & O'Connor 1997; Wang & Hutter 1998; Hodges *et al.* 2000; Rueda, Schladow & Pálmarsson 2003). Nevertheless, the linear hydrostatic model is still a most useful theoretical tool because of its simplicity, and also because of its use for numerical or experimental validation. Application of the dispersion relation for a circular basin of uniform depth is widely used for comparing the wave frequency spectrum obtained from field, laboratory or numerical experiments. Specifically, gross energetics defined by the model have been applied to Lake Kinneret to estimate the dissipation time scale (Antenucci & Imberger 2001). Also, the model was recently applied to study horizontal transport of fluid particles for various wind-forcing parameters, and chaotic advection of particles was explored (Stocker & Imberger 2003).

The linear model, however, is valid only if the amplitude of fluid motion is sufficiently small relative to the controlling vertical length scale. Nonlinear effects in internal fluid responses have been well studied in a non-rotating frame, by which the physics is isolated from the effect of the Earth's rotation. Such studies allow one to eliminate the lateral horizontal coordinate from consideration, greatly facilitating the development of reduced models amenable to rapid simulation (viz. Sakai & Redekopp 2010). It has been well recognized that a wave of finite amplitude steepens as it propagates, and the front subsequently generates a train of oscillatory waves following its own tail (Hunkins & Fliegel 1973; Farmer 1978; Horn, Imberger & Ivey 2001; Stashchuk, Vlasenko & Hutter 2005, etc.). Such sub-basin-scale waves shoal at sloping boundaries, spatially confined regions where they further steepen and break due to strong nonlinear advection, dissipating much of their energy through bottom friction and turbulent mixing (Helfrich 1992; Michallet & Ivey 1999; Vlasenko & Hutter 2002; Boegman, Ivey & Imberger 2005*a*). Energy transfer among vertical modes is also an important nonlinear process which has drawn much attention in recent years (Hüttemann & Hutter 2001; Vlasenko & Hutter 2001; Gerkema 2003; Sakai & Redekopp 2009*b*). These nonlinear effects have important implications for the lake ecology by driving transport of biological and chemical particles.

Basin-scale waves having large amplitude (i.e. of the order of 10 metres) are often observed in large lakes. In this study we intend to explore the nonlinear effects in basin-scale fluid motions in a rotating frame through an asymptotic modelling approach. In § 2 we formulate a weakly nonlinear weakly dispersive wind-forced evolution model for a circular lake of variable depth. A circular lake boundary is chosen for numerical simplicity and to isolate the essential intrinsic physics of rotating lakes from the geometric effect of radial variation of the shore boundary. In § 3 we present a summary of the linear hydrostatic model to provide preliminaries for the rest of the study. The nonlinear evolution model developed here can be solved only numerically, and the method is described briefly in § 4. Following preliminary considerations on the multi-vertical-mode model in § 5, we apply in § 6 the model to initial-value problems for Kelvin and Poincaré waves separately, exploring their evolution characteristics for different Burger numbers, amplitudes, lake dimensions and topographies. In § 7 we apply the model to wind-forced problems to determine the dominant wave modes emerging under natural forcing, and then also estimate their energy partition. We summarize the study in § 8, offering some general perspectives based on results obtained in this study.

2. Model formulation

We consider a stable continuously stratified water body confined in a cylindrical lake of variable depth. Wind stress is applied over the lake surface where we impose a slip-free rigid-lid boundary condition to eliminate the barotropic wave mode from consideration. For the primitive equations used in this study, we choose the Boussinesq-approximated inviscid equations of motion for the hydrodynamic field perturbed from the hydrostatic state. We write the equations in the form

$$\left.\begin{aligned}
&\nabla\cdot\boldsymbol{u}=0,\\
&\frac{\partial\boldsymbol{u}}{\partial t}+\boldsymbol{f}\times\boldsymbol{u}+(\boldsymbol{u}\cdot\nabla)\boldsymbol{u}=-\nabla p+\frac{\partial\boldsymbol{\tau}_h}{\partial z}-\sigma\boldsymbol{e}_z,\\
&\frac{\partial\sigma}{\partial t}+\boldsymbol{u}\cdot\nabla\sigma=\mathcal{N}^2 w,
\end{aligned}\right\}\tag{2.1}$$

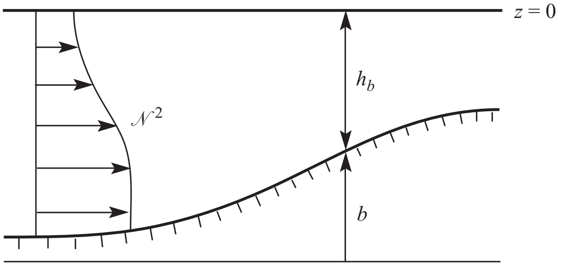

FIGURE 2. Variable depth model.

where the velocity field is $\boldsymbol{u}=u\boldsymbol{e}_r+v\boldsymbol{e}_\theta+w\boldsymbol{e}_z$, the Coriolis vector is $\boldsymbol{f}=f\boldsymbol{e}_z$, the density-divided pressure is p, the density-divided horizontal stress is $\boldsymbol{\tau}_h=\tau_r\boldsymbol{e}_r+\tau_\theta\boldsymbol{e}_\theta$, the perturbed buoyancy is $\sigma=\rho g/\rho_0$ and the Brunt–Väisälä frequency $\mathcal{N}$ is defined as

$$\mathcal{N}^2(z)=-\frac{g}{\rho_0}\frac{\mathrm{d}\rho_s(z)}{\mathrm{d}z}. \tag{2.2}$$

Solutions to (2.1) are dictated by free-slip impermeable boundary conditions at all the basin boundary surfaces, namely

$$\left.\begin{aligned} &w=0 && \text{at } z=0,\\ &\boldsymbol{u}\cdot\nabla[z-b(r,\theta)]=0 && \text{at } z=-h_b(r,\theta),\\ &u=0 && \text{at } r=r_0, \end{aligned}\right\} \tag{2.3}$$

where r_0 is the radius of the lake, h_b is the total depth function and b is the height of the topography measured from a reference horizontal surface (see figure 2). We assume that h_b (or b) varies slowly in space relative to the average depth.

We apply a long-wave scaling to the radial coordinate, time and the Coriolis parameter, defining the scaled quantities

$$(R,T)=\mu(r,t), \quad f=\mu\mathcal{F}, \tag{2.4}$$

where $\mu(\ll 1)$ is the long-wave scaling parameter. The scaling of f is introduced so that the Coriolis force affects the dynamics at the leading-order approximation. Assuming further that the depth variation is slow on the scale of the typical wavelength, we introduce a slow space radial coordinate ξ,

$$\xi=\mu^3 r. \tag{2.5}$$

After introducing these scaled variables, we expand the dependent variables in an asymptotic series by use of the amplitude parameter ϵ $(\epsilon \ll 1)$:

$$\left.\begin{aligned} &(u,v,p,\sigma)=\epsilon\left(u^{(1)},v^{(1)},p^{(1)},\sigma^{(1)}\right)+\epsilon^2\left(u^{(2)},\cdots\right)+\cdots,\\ &w=\mu\epsilon\left(w^{(1)}+\epsilon w^{(2)}+\cdots\right),\\ &\tau_{r,\theta}=\mu^3\epsilon\left(\tau_{r,\theta}^{(1)}+\epsilon\tau_{r,\theta}^{(2)}+\cdots\right). \end{aligned}\right\} \tag{2.6}$$

Further, we introduce the Korteweg–de Vries (KdV) scaling, $\epsilon=\mu^2$, in order for weak nonlinearity and the leading non-hydrostatic correction to balance in the same order.

The leading-order balance gives a linear hydrostatic model:

$$\left.\begin{aligned}
&\frac{\partial u^{(1)}}{\partial R}+\frac{u^{(1)}}{R}+\frac{1}{R}\frac{\partial v^{(1)}}{\partial \theta}+\frac{\partial w^{(1)}}{\partial z}=0,\\
&\frac{\partial u^{(1)}}{\partial T}-\mathscr{F}v^{(1)}=-\frac{\partial p^{(1)}}{\partial R},\\
&\frac{\partial v^{(1)}}{\partial T}+\mathscr{F}u^{(1)}=-\frac{1}{R}\frac{\partial p^{(1)}}{\partial \theta},\\
&\frac{\partial p^{(1)}}{\partial z}-\sigma^{(1)}=0,\\
&\frac{\partial \sigma^{(1)}}{\partial T}-\mathscr{N}^2(z)w^{(1)}=0.
\end{aligned}\right\} \tag{2.7}$$

From (2.7), combining the horizontal divergence and curl of the horizontal momentum equations, and eliminating $p^{(1)}$ and $\sigma^{(1)}$ using the vertical momentum and continuity equations, one obtains the linear long internal wave equation

$$\frac{\partial^2}{\partial T^2}\left(\frac{\partial^2 w^{(1)}}{\partial z^2}\right)+\nabla_h^2\{\mathscr{N}^2(z)w^{(1)}\}+\mathscr{F}^2\frac{\partial^2 w^{(1)}}{\partial z^2}=0, \tag{2.8}$$

where ∇_h^2 denotes the horizontal Laplacian (i.e. $\nabla_h^2\equiv\partial^2/\partial R^2+R^{-1}\partial/\partial R+R^{-2}\partial^2/\partial\theta^2$). We note that $w^{(1)}$ vanishes at both the upper and the lower boundaries. Customarily, one can seek a solution for $w^{(1)}$ in terms of a slowly varying vertical eigenfunction:

$$w^{(1)}\sim W(R,\xi,\theta,T)\phi(\xi,\theta,z). \tag{2.9}$$

Substituting (2.9) into (2.8), and after enforcing periodicity on $\mathscr{N}^2\phi$ in the azimuthal (θ) direction, we obtain the eigenvalue problem

$$\phi_l''+\frac{\mathscr{N}^2(z)}{c_l^2(\xi,\theta)}\phi_l=0;\quad \phi_l|_{z=0}=\phi_l|_{z=-h_b}=0;\quad l=1,2,\cdots. \tag{2.10}$$

The quantities c_l and ϕ_l are the eigenvalue (vertical modal phase speed) and corresponding eigenfunction, respectively, and the prime denotes a vertical derivative ($\phi'\equiv\partial\phi/\partial z$). Equation (2.10) is an ordinary differential equation (ODE) along a vertical line for a fixed horizontal coordinate, and it possesses the orthogonality relation

$$\int_{-h_b}^{0}\phi_k'\phi_l'\,\mathrm{d}z=\frac{I_l}{c_l^2}\delta_{kl};\quad \int_{-h_b}^{0}\mathscr{N}^2\phi_k\phi_l\,\mathrm{d}z=I_l\delta_{kl};\quad I_l=\int_{-h_b}^{0}\mathscr{N}^2\phi_l^2\,\mathrm{d}z, \tag{2.11}$$

where δ_{kl} is Kroneker's delta.

It is convenient to expand all dependent variables in (2.7) by using the eigenfunction in the form:

$$\left.\begin{aligned}
&u^{(1)}=\sum_l U_l^{(1)}(R,\xi,\theta,T)\phi_l'(\xi,\theta,z);\quad v^{(1)}=\sum_l V_l^{(1)}\phi_l',\\
&w^{(1)}=\sum_l W_l^{(1)}\phi_l;\quad p^{(1)}=\sum_l P_l^{(1)}\phi_l';\quad \sigma^{(1)}=\sum_l Z_l^{(1)}\mathscr{N}^2(z)\phi_l.
\end{aligned}\right\} \tag{2.12}$$

After substituting (2.12) into (2.7), and using (2.11), and then eliminating P_l and W_l, we obtain a set of evolution equations for the velocity amplitudes (U_l and V_l) and the isopycnal amplitude (Z_l):

$$\left.\begin{aligned}
&\frac{\partial U_l^{(1)}}{\partial T} - \mathscr{F} V_l^{(1)} + c_l^2 \frac{\partial Z_l^{(1)}}{\partial R} = 0,\\
&\frac{\partial V_l^{(1)}}{\partial T} + \mathscr{F} U_l^{(1)} + \frac{c_l^2}{R}\frac{\partial Z_l^{(1)}}{\partial \theta} = -\sum_{l'} \left\{ \delta_{ll'} \frac{\partial c_l^2}{\partial \theta} + \alpha_{ll'}^{(\theta)} c_l^2 \right\} \frac{Z_{l'}^{(1)}}{R},\\
&\frac{\partial Z_l^{(1)}}{\partial T} + \frac{\partial U_l^{(1)}}{\partial R} + \frac{U_l^{(1)}}{R} + \frac{1}{R}\frac{\partial V_l^{(1)}}{\partial \theta} = -\sum_{l'} \alpha_{ll'}^{(\theta)} \frac{V_{l'}^{(1)}}{R},
\end{aligned}\right\} \tag{2.13}$$

where $\alpha_{ll'}^{(\theta)}$ is defined as

$$\alpha_{ll'}^{(\theta)} = \left\langle \phi_l' \frac{\partial \phi_{l'}'}{\partial \theta} \right\rangle \equiv \frac{c_l^2}{I_l} \int_{-h_b}^{0} \phi_l' \frac{\partial \phi_{l'}'}{\partial \theta}\, \mathrm{d}z. \tag{2.14}$$

In (2.13), summation terms are modal coupling terms resulting from variable depth in the azimuthal direction. Proceeding with the next order balance in (2.1) gives

$$\left.\begin{aligned}
&\frac{\partial u^{(2)}}{\partial R} + \frac{u^{(2)}}{R} + \frac{1}{R}\frac{\partial v^{(2)}}{\partial \theta} + \frac{\partial w^{(2)}}{\partial z} = -\frac{\partial u^{(1)}}{\partial \xi},\\
&\frac{\partial u^{(2)}}{\partial T} - \mathscr{F} v^{(2)} + \frac{\partial p^{(2)}}{\partial R} = -\frac{\partial p^{(1)}}{\partial \xi} - \left[\left(\boldsymbol{u}^{(1)} \cdot \nabla\right)\boldsymbol{u}^{(1)}\right] \cdot \boldsymbol{e}_r + \frac{\partial \tau_r^{(1)}}{\partial z},\\
&\frac{\partial v^{(2)}}{\partial T} + \mathscr{F} u^{(2)} + \frac{1}{R}\frac{\partial p^{(2)}}{\partial \theta} = -\left[\left(\boldsymbol{u}^{(1)} \cdot \nabla\right)\boldsymbol{u}^{(1)}\right] \cdot \boldsymbol{e}_\theta + \frac{\partial \tau_\theta^{(1)}}{\partial z},\\
&\frac{\partial p^{(2)}}{\partial z} + \sigma^{(2)} = -\frac{\partial w^{(1)}}{\partial T},\\
&\frac{\partial \sigma^{(2)}}{\partial T} - \mathscr{N}^2 w^{(2)} = -\boldsymbol{u}^{(1)} \cdot \nabla \sigma^{(1)}.
\end{aligned}\right\} \tag{2.15}$$

The second-order boundary conditions for $w^{(2)}$ are

$$\left.\begin{aligned}
&w^{(2)} = 0 && \text{at } z = 0,\\
&w^{(2)} = u^{(1)}\frac{\partial b}{\partial \xi} + \frac{v^{(1)}}{\xi}\frac{\partial b}{\partial \theta} && \text{at } z = -h_b.
\end{aligned}\right\} \tag{2.16}$$

Both weakly nonlinear terms and the leading non-hydrostatic term ($\partial w^{(1)}/\partial T$) appear in (2.15) owing to use of the KdV scaling. The leading-order effect of variable depth now appears in (2.16) explicitly. Without argument, we simply expand $u^{(2)}$, $v^{(2)}$, $p^{(2)}$ and $\sigma^{(2)}$ in a similar way in terms of the leading-order variables as shown in (2.12). However, $w^{(2)}$ in the first equation (mass conservation) in (2.15) cannot be expanded by ϕ_l, because ϕ_l does not satisfy (2.16) at $z = -h_b$. Thereby, when applying the orthogonality relation to the mass conservation equation, we integrate the $\partial w^{(2)}/\partial z$ term via integration by parts applying (2.16). The remaining integral can be easily evaluated after eliminating $w^{(2)}$ by using the last equation in (2.15). Except for the handling of the $w^{(2)}$ term in such a way, we follow the same procedure as in the derivation of (2.13). After some algebra, we find the counterpart as follows:

$$\begin{aligned}
\frac{\partial U_l^{(2)}}{\partial T} - \mathscr{F} V_l^{(2)} + c_l^2 \frac{\partial Z_l^{(2)}}{\partial R} = {}& -c_l^2 \frac{\partial Z_l^{(1)}}{\partial \xi} - \sum_{l'} \left\{ \delta_{ll'} \frac{\partial c_l^2}{\partial \xi} + \alpha_{ll'}^{(r)} c_{l'}^2 \right\} Z_{l'}^{(1)}\\
& - \sum_{l'l''} \left\{ \beta_{ll'l''}^{(u,v)} \left(U_{l'}^{(1)} \frac{\partial U_{l''}^{(1)}}{\partial R} + \frac{V_{l'}^{(1)}}{R}\frac{\partial U_{l''}^{(1)}}{\partial \theta} - \frac{V_{l'}^{(1)} V_{l''}^{(1)}}{R} \right) \right.
\end{aligned}$$

$$
\begin{aligned}
&\left. + \beta^{(w)}_{ll'l''} D^{(1)}_{l'} U^{(1)}_{l''} + \beta^{(\theta)}_{ll'l''} \frac{V^{(1)}_{l'} U^{(1)}_{l''}}{R} + \beta^{(w)}_{ll'l''} \sum_{l'''} \alpha^{(\theta)}_{l'l'''} \frac{V^{(1)}_{l'''} U^{(1)}_{l''}}{R} \right\} \\
&+ \sum_{l'} \frac{\partial}{\partial T} \left\{ \gamma^{(w)}_{ll'} \frac{\partial D^{(1)}_{l'}}{\partial R} + \gamma^{(\alpha_1)}_{ll'} \left(\frac{1}{R} \frac{\partial V^{(1)}_{l'}}{\partial R} - \frac{V^{(1)}_{l'}}{R^2} \right) \right\} \\
&+ \frac{c_l^2}{I_l} \left\{ \phi'_l \tau^{(1)}_r \big|_{z=0} - \phi'_l \tau^{(1)}_r \big|_{z=-h_b} \right\} + \frac{1}{c_l^2} \langle \mathcal{N}^2 \phi_l \tau^{(1)}_r \rangle, \qquad (2.17a)
\end{aligned}
$$

$$
\begin{aligned}
\frac{\partial V^{(2)}_l}{\partial T} + \mathscr{F} U^{(2)}_l + \frac{c_l^2}{R} \frac{\partial Z^{(2)}_l}{\partial \theta} = &- \sum_{l'} \left\{ \delta_{ll'} \frac{\partial c_l^2}{\partial \theta} + \alpha^{(\theta)}_{ll'} c_{l'}^2 \right\} \frac{Z^{(2)}_{l'}}{R} - \sum_{l'l''} \left\{ \beta^{(u,v)}_{ll'l''} \left(U^{(1)}_{l'} \frac{\partial V^{(1)}_{l''}}{\partial R} \right.\right. \\
&\left. + \frac{V^{(1)}_{l'}}{R} \frac{\partial V^{(1)}_{l''}}{\partial \theta} + \frac{U^{(1)}_{l'} V^{(1)}_{l''}}{R} \right) + \beta^{(w)}_{ll'l''} D^{(1)}_{l'} V^{(1)}_{l''} + \beta^{(\theta)}_{ll'l''} \frac{V^{(1)}_{l'} V^{(1)}_{l''}}{R} \\
&\left. + \beta^{(w)}_{ll'l''} \sum_{l'''} \alpha^{(\theta)}_{l'l'''} \frac{V^{(1)}_{l'''} V^{(1)}_{l''}}{R} \right\} + \sum_{l'} \frac{\partial}{\partial T} \left\{ \gamma^{(w)}_{ll'} \frac{1}{R} \frac{\partial D^{(1)}_{l'}}{\partial \theta} \right. \\
&\left. + \gamma^{(\alpha_2)}_{ll'} \frac{D^{(1)}_{l'}}{R} + \gamma^{(\alpha_1)}_{ll'} \frac{1}{R^2} \frac{\partial V^{(1)}_{l'}}{\partial \theta} + \gamma^{(\alpha_3)}_{ll'} \frac{V^{(1)}_{l'}}{R^2} \right\} \\
&+ \frac{c_l^2}{I_l} \left\{ \phi'_l \tau^{(1)}_\theta \Big|_{z=0} - \phi'_l \tau^{(1)}_\theta \Big|_{z=-h_b} \right\} + \frac{1}{c_l^2} \langle \mathcal{N}^2 \phi_l \tau^{(1)}_\theta \rangle, \qquad (2.17b)
\end{aligned}
$$

$$
\begin{aligned}
\frac{\partial Z^{(2)}_l}{\partial T} + \frac{\partial U^{(2)}_l}{\partial R} + \frac{U^{(2)}_l}{R} + \frac{1}{R} \frac{\partial V^{(2)}_l}{\partial \theta} = &- \frac{\partial U^{(1)}_l}{\partial \xi} + \sum_{l'} \left\{ \frac{c_l^2}{I_l} \left[\phi'_l \phi'_{l'} \frac{\partial b}{\partial \xi} \right]_{z=-h_b} - \alpha^{(r)}_{ll'} \right\} U^{(1)}_{ll'} \\
&+ \sum_{l'} \left\{ \frac{c_l^2}{I_l} \left[\phi'_l \phi'_{l'} \frac{\partial b}{\partial \theta} \right]_{z=-h_b} \frac{V^{(1)}_{l'}}{\xi} - \alpha^{(\theta)}_{ll'} \frac{V^{(2)}_{l'}}{R} \right\} \\
&- \sum_{l'l''} \left\{ \sigma^{(u,v)}_{ll'l''} \left(U^{(1)}_{l'} \frac{\partial Z^{(1)}_{l''}}{\partial R} + \frac{V^{(1)}_{l'}}{R} \frac{\partial Z^{(1)}_{l''}}{\partial \theta} \right) - \sigma^{(w)}_{ll'l''} D^{(1)}_{l'} Z^{(1)}_{l''} \right. \\
&\left. + \sigma^{(\theta)}_{ll'l''} \frac{V^{(1)}_{l'} Z^{(1)}_{l''}}{R} - \sigma^{(w)}_{ll'l''} \sum_{l'''} \alpha^{(\theta)}_{l'l'''} \frac{V^{(1)}_{l'''} Z^{(1)}_{l''}}{R} \right\}, \qquad (2.17c)
\end{aligned}
$$

where,

$$
D^{(1)}_l = \frac{\partial U^{(1)}_l}{\partial R} + \frac{U^{(1)}_l}{R} + \frac{1}{R} \frac{\partial V^{(1)}_l}{\partial \theta}, \quad \alpha^{(r)}_{ll'} = \left\langle \phi'_l \frac{\partial \phi'_{l'}}{\partial \xi} \right\rangle, \qquad (2.18a, b)
$$

$$
\beta^{(u,v)}_{ll'l''} = \langle \phi'_l \phi'_{l'} \phi'_{l''} \rangle, \quad \beta^{(w)}_{ll'l''} = \left\langle \phi'_l \phi_{l'} \frac{\mathcal{N}^2}{c_{l''}^2} \phi_{l''} \right\rangle, \quad \beta^{(\theta)}_{ll'l''} = \left\langle \phi'_l \phi'_{l'} \frac{\partial \phi_{l''}}{\partial \theta} \right\rangle, \qquad (2.18c\text{–}e)
$$

$$
\sigma^{(u,v)}_{ll'l''} = \left\langle \frac{\phi_l}{c_l^2} \phi'_{l'} \mathcal{N}^2 \phi_{l''} \right\rangle, \quad \sigma^{(w)}_{ll'l''} = \left\langle \frac{\phi_l}{c_l^2} \phi_{l'} (\mathcal{N}^2 \phi_{l''})' \right\rangle, \qquad (2.18f, g)
$$

$$
\sigma^{(\theta)}_{ll'l''} = \left\langle \frac{\phi_l}{c_l^2} \phi_{l'} \mathcal{N}^2 \frac{\partial \phi_{l''}}{\partial \theta} \right\rangle, \quad \gamma^{(w)}_{ll'} = \langle \phi_l \phi_{l'} \rangle, \quad \gamma^{(\alpha_1)}_{ll'} = \sum_{l''} \gamma^{(w)}_{ll''} \alpha^{(\theta)}_{l''l'}, \qquad (2.18h\text{–}j)
$$

$$
\gamma^{(\alpha_2)}_{ll'} = \frac{\partial \gamma^{(w)}_{ll'}}{\partial \theta} + \gamma^{(\alpha_1)}_{ll'}, \quad \gamma^{(\alpha_3)}_{ll'} = \frac{\partial \gamma^{(\alpha_1)}_{ll'}}{\partial \theta} + \sum_{l''} \alpha^{(\theta)}_{ll''} \gamma^{(\alpha_1)}_{l''l'}. \qquad (2.18k, l)
$$

Equations (2.17*a–c*) contain weak nonlinearity, a weak non-hydrostatic (dispersive) effect, a slowly varying depth effect, wind stress and bottom friction in the same order. These terms are all coupled, implying energy transfer among all vertical modes. Modal coupling of nonlinear terms is expressed by double and triple sums. With spatially variable coefficients, the behaviour of these nonlinear terms is undoubtedly expected to be quite complicated. The coefficients of topographic coupling terms $\alpha_{ll'}^{(r)}$ in (2.18*a–l*) and $\alpha_{ll'}^{(\theta)}$ in (2.14) can be further simplified into a computationally efficient form as given by our earlier work (Sakai & Redekopp 2009*b*). A general derivation of the topographic coupling coefficients for wave propagation over varying topographies has been developed by Griffiths & Grimshaw (2007) in their study of the internal tide in continental shelf regions.

In order to expose the basic set of parameters underlying the evolution model given in (2.17), we introduce characteristic scales for the dependent and independent variables and form dimensionless equivalents of (2.17). However, both for brevity of presentation and for specific reference in later sections, only the dimensionless equations for the evolution of a single vertical mode will be presented here. The resulting set of equations is:

$$\begin{aligned}\frac{\partial U}{\partial t} - \mathscr{B}V + \frac{\partial}{\partial r}(c^2 Z) = {} & -c^2\alpha^{(r)}Z - \left\{\beta^{(u,v)}\left(U\frac{\partial U}{\partial r} + \frac{V}{r}\frac{\partial U}{\partial \theta} - \frac{V^2}{r}\right)\right. \\ & \left. + \beta^{(w)}DU + \beta^{(\theta,w)}\frac{VU}{r}\right\} + \Lambda^2\frac{\partial}{\partial t}\left\{\gamma^{(w)}\frac{\partial D}{\partial r}\right. \\ & \left. + \gamma^{(\alpha_1)}\left(\frac{1}{r}\frac{\partial V}{\partial r} - \frac{V}{r^2}\right)\right\} + \frac{k_s}{\mathscr{W}}\tau_r, \qquad (2.19a)\end{aligned}$$

$$\begin{aligned}\frac{\partial V}{\partial t} + \mathscr{B}U + \frac{1}{r}\frac{\partial}{\partial \theta}(c^2 Z) = {} & -c^2\alpha^{(\theta)}\frac{Z}{r} - \left\{\beta^{(u,v)}\left(U\frac{\partial V}{\partial r} + \frac{V}{r}\frac{\partial V}{\partial \theta} + \frac{UV}{r}\right)\right. \\ & \left. + \beta^{(w)}DV + \beta^{(\theta,w)}\frac{V^2}{r}\right\} + \Lambda^2\frac{\partial}{\partial t}\left\{\gamma^{(w)}\frac{1}{r}\frac{\partial D}{\partial \theta} + \gamma^{(\alpha_2)}\frac{D}{r}\right. \\ & \left. + \gamma^{(\alpha_1)}\frac{1}{r^2}\frac{\partial V}{\partial \theta} + \gamma^{(\alpha_3)}\frac{V}{r^2}\right\} + \frac{k_s}{\mathscr{W}}\tau_\theta, \qquad (2.19b)\end{aligned}$$

$$\begin{aligned}\frac{\partial Z}{\partial t} + \frac{\partial U}{\partial r} + \frac{U}{r} + \frac{1}{r}\frac{\partial V}{\partial \theta} = {} & \kappa^{(r)}U + \kappa^{(\theta)}\frac{V}{r} - \left\{\sigma^{(u,v)}\left(U\frac{\partial Z}{\partial r} + \frac{V}{r}\frac{\partial Z}{\partial \theta}\right)\right. \\ & \left. - \sigma^{(w)}DZ + \sigma^{(\theta,w)}\frac{VZ}{r}\right\}, \qquad (2.19c)\end{aligned}$$

where all vertical modal indices are dropped, and additional coefficients are defined as

$$\left.\begin{aligned}&\beta^{(\theta,w)} = \beta^{(\theta)} + \beta^{(w)}\alpha^{(\theta)}, \quad \sigma^{(\theta,w)} = \sigma^{(\theta)} - \sigma^{(w)}\alpha^{(\theta)}, \quad k_s = \frac{c^2}{I}\phi'|_{z=0}, \\ &\kappa^{(r)} = \frac{1}{I}\,(\phi')^2|_{z=-h_b} \times \frac{\partial b}{\partial r} - \alpha^{(r)}, \quad \kappa^{(\theta)} = \frac{1}{I}\,(\phi')^2|_{z=-h_b} \times \frac{\partial b}{\partial \theta} - \alpha^{(\theta)}.\end{aligned}\right\} \qquad (2.20)$$

In these equations we scale r by the lake radius r_0, z and Z by the epilimnion (mixing layer) depth h_1, $\mathscr{N}$ by its maximum value $\mathscr{N}_0$, t by $r_0/\mathscr{N}_0 h_1$, c by $\mathscr{N}_0 h_1$, U and V by $\mathscr{N}_0 h_1^2$ and $\tau_{r,\theta}|_{z=0}$ by u_{*0}^2, where u_{*0} is a surface friction velocity induced by the wind stress.

There are three important dimensionless parameters in (2.19*a*, *b*): the Burger number $\mathscr{B}$, the Wedderburn number $\mathscr{W}$ and the aspect ratio Λ. The Burger number $\mathscr{B}$ used in this study is defined as a ratio between the lake radius r_0 and internal Rossby radius of deformation $R_0 = \mathscr{N}_0 h_1/f$:

$$\mathscr{B} = \frac{f r_0}{\mathscr{N}_0 h_1} = \frac{r_0}{R_0}. \tag{2.21}$$

The Wedderburn number is defined as a ratio between baroclinic pressure gradient and the wind stress:

$$\mathscr{W} = \frac{\mathscr{N}_0^2 h_1^3}{u_{*0}^2 r_0}. \tag{2.22}$$

The aspect ratio Λ in (2.19*a*, *b*) is defined as $\Lambda = h_1/r_0$, which quadratically scales the dispersive terms. The vertical structure of the stratification and the non-uniform depth are implicitly included in the linear phase speed c and in each integral coefficient defined in (2.18*a*, *b*) and (2.20).

In the formation of (2.19) from (2.17), we have neglected the bottom friction term ($\tau_{r,\theta}|_{z=-h_b} = 0$), and also assumed that the wind stress decreases to zero at the base of the epilimnion (i.e. $\langle \mathscr{N}^2 \phi \tau_r \rangle = \langle \mathscr{N}^2 \phi \tau_\theta \rangle = 0$). The effect of wind stress penetration into the metalimnion was examined in Sakai & Redekopp (2009*b*), and is not pursued further here. Since we neglect the influence of bottom friction, the model should represent the wind-generated response for the order of several days, which is a typical time scale for forced internal waves in large lakes (Csanady 1968; Antenucci & Imberger 2001).

3. Linear hydrostatic model

Before proceeding to a simulation of the forced nonlinear response, we summarize the set of exact solutions to the linear hydrostatic problem for uniform depth. Although the model has been well documented (Lamb 1932; Csanady 1967), we include the results in this section since they provide essential preliminaries for the rest of this report. The model is the same as (2.13), which we write in a dimensionless form:

$$\left.\begin{aligned} \frac{\partial U}{\partial t} - \mathscr{B} V + c^2 \frac{\partial Z}{\partial r} &= 0, \\ \frac{\partial V}{\partial t} + \mathscr{B} U + c^2 \frac{1}{r}\frac{\partial Z}{\partial \theta} &= 0, \\ \frac{\partial Z}{\partial t} + \frac{\partial U}{\partial r} + \frac{U}{r} + \frac{1}{r}\frac{\partial V}{\partial \theta} &= 0. \end{aligned}\right\} \tag{3.1}$$

After constructing an equation in favour of Z, a wave-like solution is found by assuming $Z \sim \mathscr{R}(r) \exp \mathrm{i}(m\theta - \mathscr{B}\omega t)$, where ω is a dimensionless frequency scaled by f. The fundamental solution is written in the form:

$$\left.\begin{aligned} U &= -A_0 \frac{c^2}{\mathscr{B}(\omega^2 - 1)} \left\{ m\frac{\mathscr{R}(r)}{r} - \omega \mathscr{R}'(r) \right\} \sin(m\theta - \mathscr{B}\omega t - \delta_0), \\ V &= A_0 \frac{c^2}{\mathscr{B}(\omega^2 - 1)} \left\{ m\omega\frac{\mathscr{R}(r)}{r} - \mathscr{R}'(r) \right\} \cos(m\theta - \mathscr{B}\omega t - \delta_0), \\ Z &= A_0 \mathscr{R}(r) \cos(m\theta - \mathscr{B}\omega t - \delta_0), \end{aligned}\right\} \tag{3.2}$$

where A_0 is a wave amplitude, δ_0 is an initial phase of the wave and $\mathscr{R}(r)$ is a radial eigenfunction normalized by its maximum value, i.e. $\mathscr{R}(r) = \mathscr{R}^*(r)/|\mathscr{R}^*(r)|_{\max}$, where

$\mathscr{R}^*(r)$ is written in terms of the Bessel (J) or the modified-Bessel (I) function

$$\mathscr{R}^*(r) = \begin{cases} I_m(\mathscr{B}^* r) & \text{if } \omega^2 < 1, \\ J_m(\mathscr{B}^* r) & \text{if } \omega^2 > 1, \end{cases} \quad \text{and} \quad \mathscr{B}^* = \frac{\mathscr{B}}{c}\sqrt{|1-\omega^2|}, \tag{3.3}$$

where $I_m(\mathscr{B}^* r)$ is the Kelvin wave (subinertial) solution and $J_m(\mathscr{B}^* r)$ is the Poincaré wave (superinertial) solution. The radial wavenumber is implicitly contained in $\mathscr{B}^*$ through ω, which is an eigenfrequency determined by a dispersion relation, namely for the Kelvin wave mode we have

$$\mathscr{B}^* I_{m-1}(\mathscr{B}^*) - m\left(1 + \frac{1}{\omega}\right) I_m(\mathscr{B}^*) = 0. \tag{3.4}$$

Since $I_m(r)$ is a positive, increasing function, (3.4) implies that the Kelvin wave can possess only a single radial mode of positive frequency. We distinguish the wave travelling direction by using 'cyclonic' (counter-clockwise) for positive frequency and 'anti-cyclonic' (clockwise) for negative frequency (here we suppose that the frame of reference is set in the northern hemisphere). For $\omega^2 > 1$, I_m is replaced by J_m in (3.4). The dispersion relation then gives increasing frequencies in discrete radial modes for both cyclonic and anti-cyclonic waves for given azimuthal mode (m) and Burger number $\mathscr{B}$.

Dispersion relations for the first three azimuthal and radial modes are plotted in figure 1 as a function of the Burger number. For convention, we label the wave mode by the format 'M(azimuthal mode)R(radial mode)'. The dimensionless frequency $\omega = 1$ is a critical case between Kelvin and Poincaré wave modes, and the corresponding solution is easily found by assuming $(U, V, Z) \sim \exp(\mathrm{i}m\theta - \mathscr{B}t)$ in (3.1), yielding

$$\left.\begin{aligned} U &= -A_0 \frac{\mathscr{B}_c}{2(m+1)}(r^{m+1} - r^{m-1}) \sin(m\theta - \mathscr{B}_c t - \delta_0), \\ V &= A_0 \frac{\mathscr{B}_c}{2(m+1)}(r^{m+1} + r^{m-1}) \cos(m\theta - \mathscr{B}_c t - \delta_0), \\ Z &= A_0 r^m \cos(m\theta - \mathscr{B}_c t - \delta_0), \end{aligned}\right\} \tag{3.5}$$

where $\mathscr{B}_c$ is a critical Burger number

$$\mathscr{B}_c = c\sqrt{m(m+1)}, \tag{3.6}$$

that is determined by requiring $U = 0$ at $r = 1$ when deriving (3.5). The Kelvin wave solution exists only if $\mathscr{B} > \mathscr{B}_c$. It is easy to show that $\omega = -1$ is physically irrelevant, since the corresponding solution yields $Z \sim r^{-m}$, which is singular at $r = 0$.

4. Numerical method

Since our evolution model derived in § 2 is described in terms of polar coordinates, a numerical singularity is inevitable at $r = 0$, even though the solution is regular (C^∞) in the domain (Boyd 2001). We first attempted to integrate (2.19) through a finite difference approach, but it failed to continue the integration for sufficiently long time due to emergence of numerical instability on the computational grid adjacent to $r = 0$. The numerical instability, in general, is caused by the inability of such a low-order method to satisfy all necessary regularity conditions as $r \to 0$. To remedy this difficulty, we implemented the spectral method described here briefly.

Upon formulation of the spectral model, it is convenient (but not always necessary) to use radial flux variables via the transformation $r(U, V) \longmapsto (\tilde{U}, \tilde{V})$ instead of the original variables. We expand the dependent variables by a Fourier exponential in the azimuthal direction and one-sided Jacobi polynomials (Matsushima & Marcus 1995; Verkley 1997) in the radial direction. After projecting the variables onto a finite dimensional subspace, say $\{\tilde{U}, \tilde{V}, Z\} \longrightarrow \{\tilde{U}^N, \tilde{V}^N, Z^N\}$, we have that

$$\left.\begin{aligned} \tilde{U}^N &= \sum_{m=-N}^{N} \sum_{n=|m|,\, n\geqslant 1}^{N+2} \hat{u}_{mn}\{Q_{mn}(r) - \delta_{m0}(-1)^{n/2}Q_{mn}(r)\}\mathrm{e}^{\mathrm{i}m\theta}, \\ \tilde{V}^N &= \sum_{m=-N}^{N} \sum_{n=|m|,\, n\geqslant 1}^{N+2} \hat{v}_{mn}\{Q_{mn}(r) - \delta_{m0}(-1)^{n/2}Q_{mn}(r)\}\mathrm{e}^{\mathrm{i}m\theta}, \\ Z^N &= \sum_{m=-N}^{N} \sum_{n=|m|}^{N} \hat{z}_{mn} Q_{mn}(r)\mathrm{e}^{\mathrm{i}m\theta}, \end{aligned}\right\} \tag{4.1}$$

where $Q_{mn}(r)$ is the one-sided Jacobi polynomial

$$Q_{mn}(r) = r^{|m|} P_k^{(0,|m|)}(2r^2 - 1), \quad n = |m| + 2k, \quad k = 0, 1, 2\ldots, \tag{4.2}$$

and $P_k^{(0,|m|)}(x)$ is the Jacobi polynomial of order k. Also, $Q_{mn}(r)$ is an orthogonal polynomial of degree n with weight function r, namely

$$\int_0^1 Q_{mn}(r)Q_{mn'}(r)r\,\mathrm{d}r = \frac{\delta_{nn'}}{2(n+1)}. \tag{4.3}$$

The one-sided Jacobi polynomial, by its nature, implicitly satisfies the regularity condition at $r = 0$ for a scalar function (e.g. Z). However, the polynomial by itself is not satisfactory to guarantee the regularity at $r = 0$ for vector functions. Vector functions $(\tilde{U}, \tilde{V})$ that are regular at $r = 0$ dictate the use of a kinematic constraint at $r = 0$, which is written here without derivation (see Sakai & Redekopp 2009*a* for details):

$$\sum_{n=|m|}^{N+2} (-1)^k \frac{(|m| + k)!}{k!|m|!} \{\hat{u}_{mn} + \mathrm{i}\,\mathrm{sgn}(m)\hat{v}_{mn}\} = 0 \quad \text{for} \quad |m| \geqslant 1. \tag{4.4}$$

Also, the boundary condition of vanishing normal velocity ($\tilde{U} = 0$ at $r = 1$) is expressed in the spectral space as

$$\sum_{n=|m|,\, n\geqslant 1}^{N+2} \{1 - \delta_{m0}(-1)^{n/2}\}\, \hat{u}_{mn} = 0. \tag{4.5}$$

Substituting (4.1) into (2.19), and after using (4.3), plus its counterpart in the azimuthal direction, the equations are transformed to a system of first-order ODEs in time in the spectral space. Nonlinear terms in the evolution equations are first evaluated in physical space at Gauss–Legendre type collocation points in the radial direction, and uniform collocation points in the azimuthal direction. Then, these physical values are projected onto the spectral space via inverse transforms (Gaussian quadrature in radial and fast Fourier transform in azimuthal directions). Resolution of the collocation grid was chosen so that the spectral coefficients are evaluated exactly without aliasing for a given truncation N. The system of ODEs, after combining with (4.4) and (4.5), was integrated simultaneously in time by using the fourth-order Runge–Kutta scheme of fixed time step size. The numerical scheme was validated in our earlier work (Sakai & Redekopp 2009*b*) through comparisons of simulations

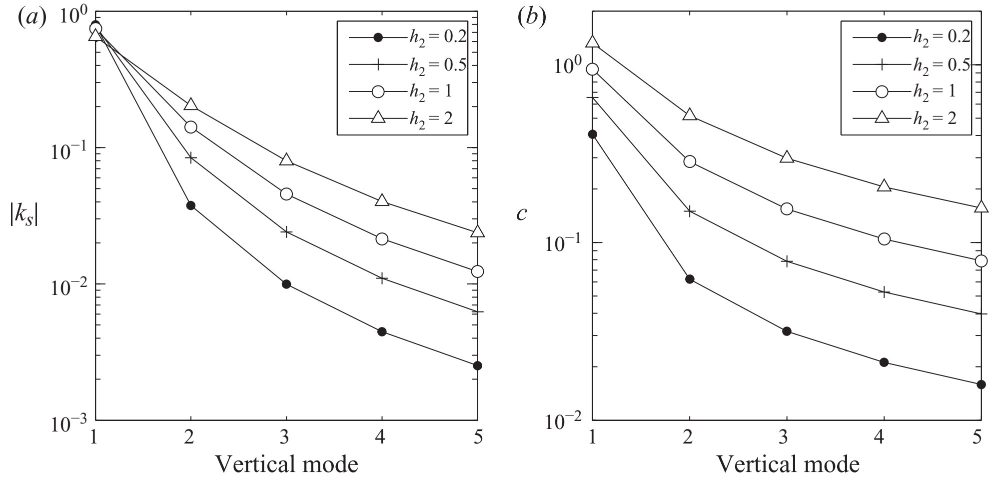

FIGURE 3. (*a*) Modal forcing coefficient k_s and (*b*) eigenspeed c as functions of vertical mode.

against the exact solution of the initial value problem for the linear hydrostatic model described in § 3.

5. Preliminary considerations

5.1. *Implications of environmental structure*

We first investigate the evolution of initial values for a circular lake of uniform depth. Vertical structure used in this study comprises an epilimnion of depth h_1 (mixing layer), a metalimnion of depth h_2 having constant density gradient (thermoclinic layer with constant Brunt–Väisälä frequency $\mathscr{N}_0$) and a hypolimnion of uniform density, which we express by the formula,

$$\mathscr{N}^2(z) = \frac{1}{2}\left\{\tanh\left(\frac{z+1+h_2}{\delta}\right) - \tanh\left(\frac{z+1}{\delta}\right)\right\}, \tag{5.1}$$

after scaling all vertical lengths by h_1 and $\mathscr{N}$ by $\mathscr{N}_0$. The parameter δ controls the thickness of transition regions at the upper and lower ends of the metalimnion. For all simulations discussed herein we use $\delta = 1/10$ and consider a total depth of $5h_1$.

Before discussing simulations of different dynamic states we examine a couple of key parameters appearing in equations (2.19). In figure 3 we present the magnitude of the modal coefficient k_s and the eigenspeed c as a function of the mode number for several metalimnion depths. It is clear that the rate of energy deposition by wind forcing into mode two, relative to that in mode one, is not strikingly disparate, particularly as the thickness of the metalimnion increases. For short-time simulations, mode one will clearly be dominant. However, the energy in mode two (and higher modes) may become significant as time increases, and therewith induce significant inter-modal nonlinear coupling. Also, the phase-speed separation between modes raises some further concerns about the severe truncation to a two-layer approximation and opens the possibility for locally enhanced nonlinear interaction after a couple inertial periods.

The variation of the coefficients of the self-modal and cross-modal terms in (2.17) with vertical structure parameters was evaluated in a different model by Sakai &

Redekopp (2009*b*). Since the coupling coefficients denoted by β here are identical with corresponding coefficients in that earlier work, we do not repeat those data here.

5.2. *Multi-mode preliminaries*

The numerical code was developed to simulate (2.17) for the nonlinear interaction of the first two vertical modes, denoted in what follows by V1 and V2 for the first and second vertical modes, respectively. It was noted in the early simulations that instabilities invariably developed in which the growth rate increased with increasing amplitude, or increasing applied wind stress, or for simulations with higher resolution, or for cases where the environmental structure yielded coefficients of the nonlinear coupling terms with larger magnitude. The observed instability was manifested in spectral space as a continual flow of energy to higher wavenumbers (both azimuthal and radial) in V2. This instability vanished when the V2 cross-modal coefficients were set to zero.

Instabilities of this nature are not uncommon in simulations of inviscid dynamics, and are usually circumvented by either of two approaches. First, a high-wavenumber filtering is applied. Such an approach could be expected to yield similar advantages in the present case, and permit stable, long-time simulations of the fully coupled, multi-mode problem. However, a spectral filtering algorithm of that sort has not yet been developed for schemes employing one-sided Jacobi polynomials in polar coordinates. Alternatively, the addition of hyperviscosity terms, a technique used quite widely in various contexts, would effectively damp the continuous (weak) flow of energy to high wavenumbers. The downside of using hyperviscosity is that it requires a drastic reduction in allowed time step relative to the inviscid simulations reported here.

With these considerations in view, we proceed to simulate the restricted case of a single vertical mode, focusing on the role of the different physical parameters and variable depth, on the nonlinear evolution of the dominant mode, V1 (viz. equations (2.19)). The flow of energy from the basin scale to higher azimuthal and radial modes of the basin is an issue of fundamental concern, and characterization of this flow in the case of a single eigenmode of the vertical structure via a computational scheme having full spectral accuracy is deemed an important base study in its own right.

Before proceeding to discuss the evolutionary characteristics of the V1 field, we first explore some potential deficiencies implicit in restricting simulations to the severely truncated model of a single vertical eigenmode. To this end, we present a set of comparative results for a fixed set of parameters in figure 4 where different modal amplitude fields are shown at three corresponding times. In obtaining these fields, a unidirectional wind stress at fixed Wedderburn number was applied for a fixed time interval of $0 < t < 0.5$ that corresponds to one-third of the inertial period with the Burger number $\mathscr{B} = 4$. The first two rows depict the isopycnal field obtained for the first two modes of the uncoupled, linear hydrostatic system. Figure 4(*a*) depicts the V2 field and figure 4(*b*) depicts the corresponding field for V1. We then exhibit in figure 4(*c*) the V1 field obtained from a simulation of the fully nonlinear equation for the V1 field when coupled with V2, but the V2 field is obtained from the entirely linear model for V2 (i.e. the V2 field as seen in figure 4*a*). That is, figure 4(*c*) provides snapshots of the V1 field including both self-nonlinear and cross-nonlinear dynamics, but the V2 coupling with V1 entails only the linear, uncoupled evolution of V2. In figure 4(*d*) we show the V1 field at corresponding times obtained from a nonlinear–dispersive simulation of V1 in the absence of any V2 field, either linear or nonlinear. Lastly, in figure 4(*e*), we show the difference field between the two V1 fields exhibited in figures 4(*c*) and 4(*d*). Hence, figure 4(*e*) depicts the ‘error’ in the restricted evolution

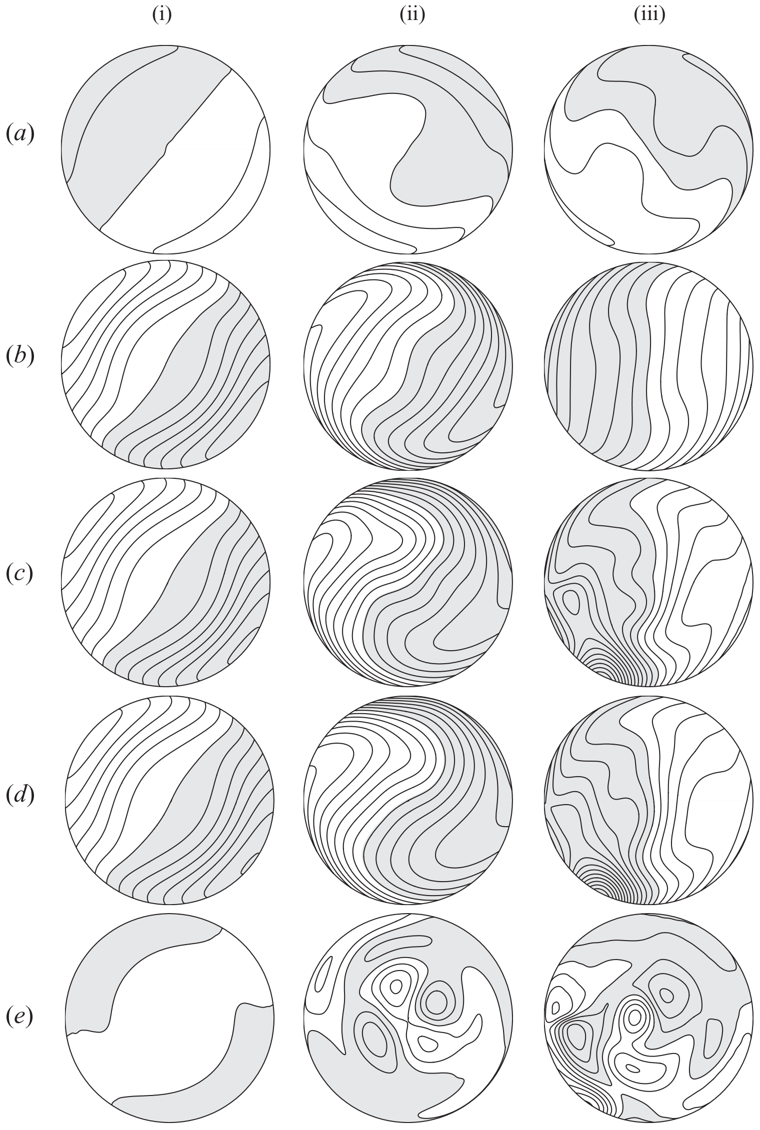

FIGURE 4. Snapshots of isopycnal amplitude Z of wind-forced two-mode responses. Rows: (*a*) V2 linear hydrostatic response, (*b*) V1 linear hydrostatic response, (*c*) V1 response (all model terms are included), (*d*) V1 self-nonlinear response and (*e*) difference between (*c*) and (*d*). Columns: (i) onset of wind stress ($t = 0.52$), (ii) $t = 20$ and (iii) $t = 40$. Contour level steps are 0.02 for (*a–d*) and 0.005 for (*e*). Grey areas represent negative values, otherwise values are positive. Maximum amplitudes at time level (iii) $t = 40$ are (*a*) ± 0.047, (*b*) ± 0.141, (*c*) -0.258, (*d*) -0.279 and (*e*) 0.031. Physical configuration for the simulation is $\mathscr{B} = 4$, $\mathscr{W} = 2.5$, $\Lambda = 0.025$, $n_s = 2$, $\kappa_w = 1/3$ (see §7 for definitions of n_s and κ_w).

of V1 arising from neglect of any coupling between V1 and V2. Of course, all coupling to higher vertical modes has also been suppressed. It is evident that the peak amplitude error in the field arising from the restricted V1-alone simulation increases slowly in time and is about 10% at $t = 40$, a time that corresponds to twenty-five inertial periods. It is important to emphasize that such errors, which are associated with local structures in the basin with quite different vertical eigenmode shapes,

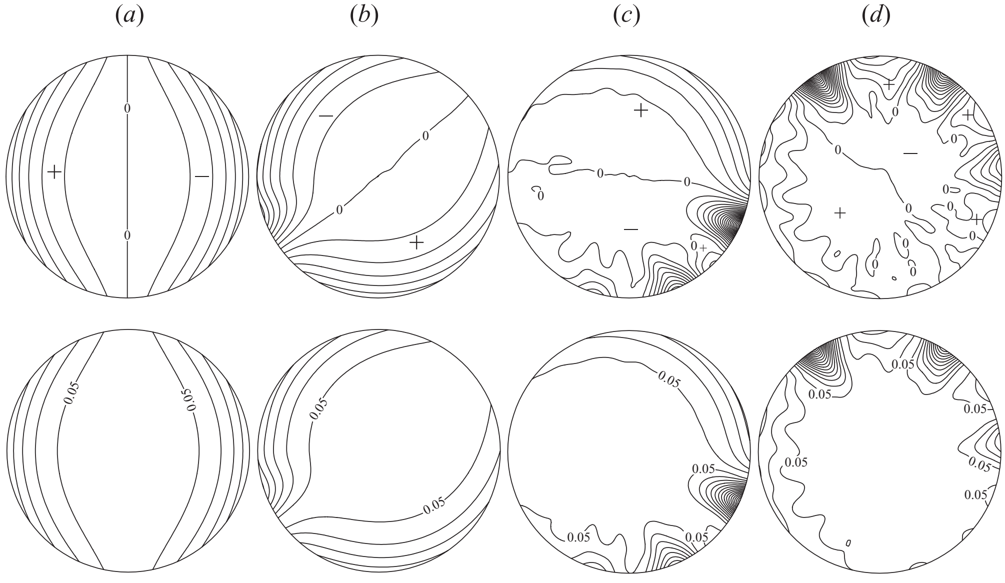

FIGURE 5. Evolution of the Kelvin wave (M1R1+). Snapshots of the isopycnal amplitude Z (upper row) and the magnitude of the velocity amplitude $\sqrt{U^2 + V^2}$ (lower row) are taken at (a) $t = 0$, (b) $t = 8$, (c) $t = 16$ and (d) $t = 24$. Contour level step is 0.05 for all the plots. The lowest contour level shown in the velocity contour plot is 0.05.

may in fact have important implications for horizontal transport in a basin. Studies of transport, as explored by Stocker & Imberger (2003) for example, are reserved for future consideration, preferably with an implemented high-wavenumber filtering scheme so that full modal coupling is included.

6. Initial value problem

We consider the dynamical model of (2.19) with the environmental state described by (5.1) with $h_2 = 1(= h_1)$, $\delta = 1/10$, and the depth of the hypolimnion $h_3 = 3$ (i.e. total depth $5h_1$). The vertical mode-one phase speed (c) is 0.9395 for this vertical structure after numerically solving (2.10) using (5.1). The corresponding vertical eigenfunction is normalized by its maximum value. Exact solutions to the linear hydrostatic model described in § 3 are used as the initial conditions. Of course, such exact solutions are not the solution of (2.19). However, at the initial stage of evolution where nonlinearity is not significant, these solutions can serve as a reasonable approximation to the model solutions.

6.1. *Evolution of a Kelvin wave on uniform depth*

In figure 5, we show a typical picture of the evolution of an azimuthal mode-one Kelvin wave (M1R1+), where we chose $\mathscr{B} = 4$, $\Lambda = 0.025$ and initial wave amplitude $A_0 = -0.3$, and we set the spectral resolution $N = 70$ and used an integration time step $\Delta t = 0.0025$. The negative side of the isopycnal amplitude (Z) propagates faster than its positive side, creating a front which gradually steepens as it travels in the cyclonic direction. (Here $t = 8 \approx 1.4T_*$, where T_* is the linear wave period. By convention T_* represents the period of either the linear Kelvin M1R1+ or Poincaré M1R1− wave mode depending on which wave mode is discussed. In the present case T_* is the period of the linear Kelvin wave.) The steep front evolves and it generates a train of shorter

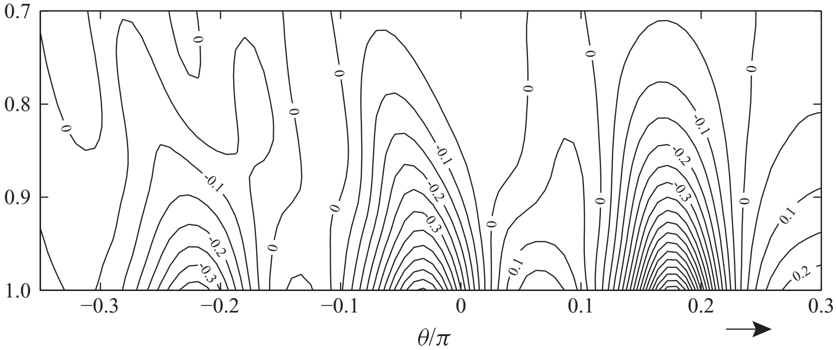

FIGURE 6. Developed view of the Kelvin wavefront (isopycnal amplitude Z for $\mathscr{B}=8$, $A_0=-0.3$, $\Lambda=0.025$, $t=18$). The front position and its propagating direction are indicated by an arrow.

waves ($t=16\approx 2.7T_*$), the leading front passes through its own oscillatory tail, and then the field becomes more complicated generating even shorter length-scale waves ($t=24\approx 4.1T_*$). A width of a linear Kelvin wave l_K can be defined in a similar way to one used in the case of an infinite channel model,

$$l_K = \left.\frac{\mathscr{R}^*(r)}{\mathscr{R}'^*(r)}\right|_{r=1} = \mathscr{B}^{*-1}\frac{I_m(\mathscr{B}^*)}{I'_m(\mathscr{B}^*)}. \tag{6.1}$$

Since $I_m(x)/I'_m(x) \to 1$ as $x \to \infty$, then $l_K \sim \mathscr{B}^{*-1}$ for large $\mathscr{B}^*$ ($=\mathscr{B}/c\sqrt{1-\omega^2} \sim \mathscr{B}/c$, after noting $\omega \ll 1$ for large $\mathscr{B}$ from figure 1). At the present Burger number, the alongshore horizontal fluid motion (see the second row of figure 5) is confined near the shore ($l_K=0.27$), and it persists even after the oscillatory waves develop. The steepening of the Kelvin wave is not a new result by itself. It has been demonstrated by several authors by utilizing nonlinear models in either semi-infinite or infinite domains. Bennett (1973) first demonstrated the steepening of Kelvin waves by analysing a transversely geostrophic shallow water model. Tomasson & Melville (1990) demonstrated a triad resonance of a periodic Kelvin wavetrain by using a weakly nonlinear dispersive model, and at the same time their numerical simulation showed steepening of Kelvin wavefronts. Fedorov & Melville (1995) demonstrated steepening and subsequent breaking of Kelvin wavefronts by using a shallow water model. Also, the steepening of Kelvin waves on the equatorial thermocline has been studied by many authors (e.g. Boyd 1998; Fedorov & Melville 2000).

Regarding the steepening of Kelvin waves, Maxworthy (1983) produced a strongly nonlinear solitary internal Kelvin wave of vertical mode two in his laboratory tank, where it was clearly shown that the crest of the wave was curved backward as it travelled along the sidewall. Melville, Tomasson & Renouard (1989) later demonstrated the backward curvature of a solitary Kelvin wave by numerically simulating a weakly nonlinear weakly dispersive model in a channel. Similar results are also found in our model simulation as shown in figure 6, where Z is developed over the r–θ plane for $\mathscr{B}=8$ at $t=18$. Lines of constant phase (troughs) curve backward relative to their travelling direction. The trough of the leading wave is less curved due to the presence of the steep front, but troughs of following waves are clearly curved backward. This curvature is due to the nonlinear effect on the wave phase speed (i.e. waves of larger amplitude travel faster than those of smaller amplitude). In figure 7 the azimuthal location of the minimum value of Z is plotted as a function of time for

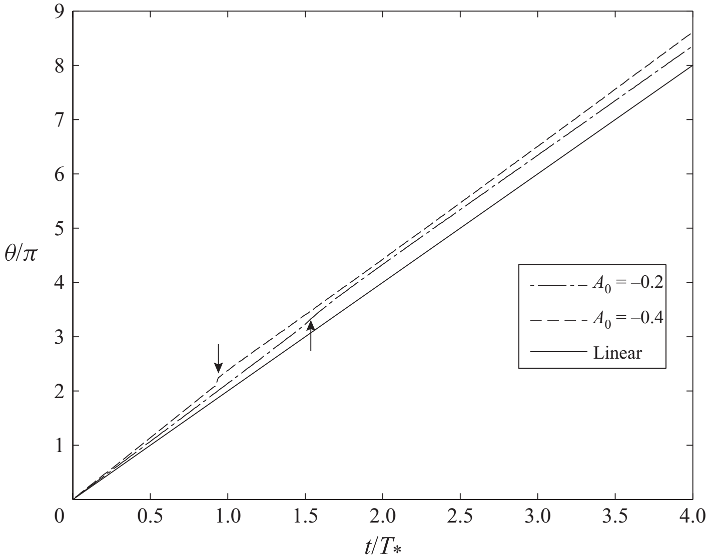

FIGURE 7. Azimuthal location of the minimum value of the isopycnal amplitude Z (the leading Kelvin wave trough) as a function of time.

different wave amplitudes, showing that the wave of larger amplitude travels faster. Small jumps at $t \approx T_*$ for $A_0 = -0.4$ and at $t \approx 1.5T_*$ for $A_0 = -0.2$, indicated by arrows in the figure, implicitly indicate the emergence of oscillatory waves, where the minimum point of Z quickly shifts from the middle of the wave trough to the trough of the leading oscillatory wave following the steepened front.

The rate of steepening of a Kelvin wave is a strong function of amplitude and environmental parameters (i.e. the vertical structure, $\mathscr{B}$ and Λ). To quantify this, we calculated the maximum azimuthal gradient of the Z field along the basin perimeter for various sets of parameters. Figure 8(a) shows the gradient of the wavefront as a function of time for different initial amplitudes for fixed $\mathscr{B} = 4$ and $\Lambda = 0.025$. Calculated gradients are normalized by their initial values and amplitudes. The figure exhibits that waves of larger amplitude steepen quickly, reaching a maximum gradient, where the gradient does not increase any more owing to the balance between nonlinear and dispersive effects. Dependence of the steepening rate on the initial amplitude presented here is consistent with that in earlier work by Ripa (1982) on the steepening of Kelvin waves on the equatorial β-plane and by Horn *et al.* (2001) on one-dimensional (non-rotating) progressive waves. Figure 8(b) shows the gradient of the wavefront as a function of time for various values of $\mathscr{B}$ for fixed $A_0 = -0.3$ and $\Lambda = 0.025$. Calculated gradients are normalized by their initial values. The rate of steepening is significantly modified when $\mathscr{B}$ is relatively small ($\mathscr{B} < 2$), resulting in a slower steepening rate for smaller $\mathscr{B}$. But the wave does not steepen any more if $\mathscr{B} < \mathscr{B}_c$, where the wave becomes superinertial (Poincaré type), although the propagation direction of the wave is still cyclonic, the same as that of a Kelvin wave. For a small lake where the effect of the Earth's rotation is negligible (i.e. $\mathscr{B} \rightarrow 0$), the eigenfrequencies of both the cyclonic wave mode and the anti-cyclonic counterpart become identical. When such a small lake is subject to uniform wind stress, both rotating waves can be equally excited by the wind stress, resulting in basin-scale standing waves oriented along a single (wind) direction in the absence of

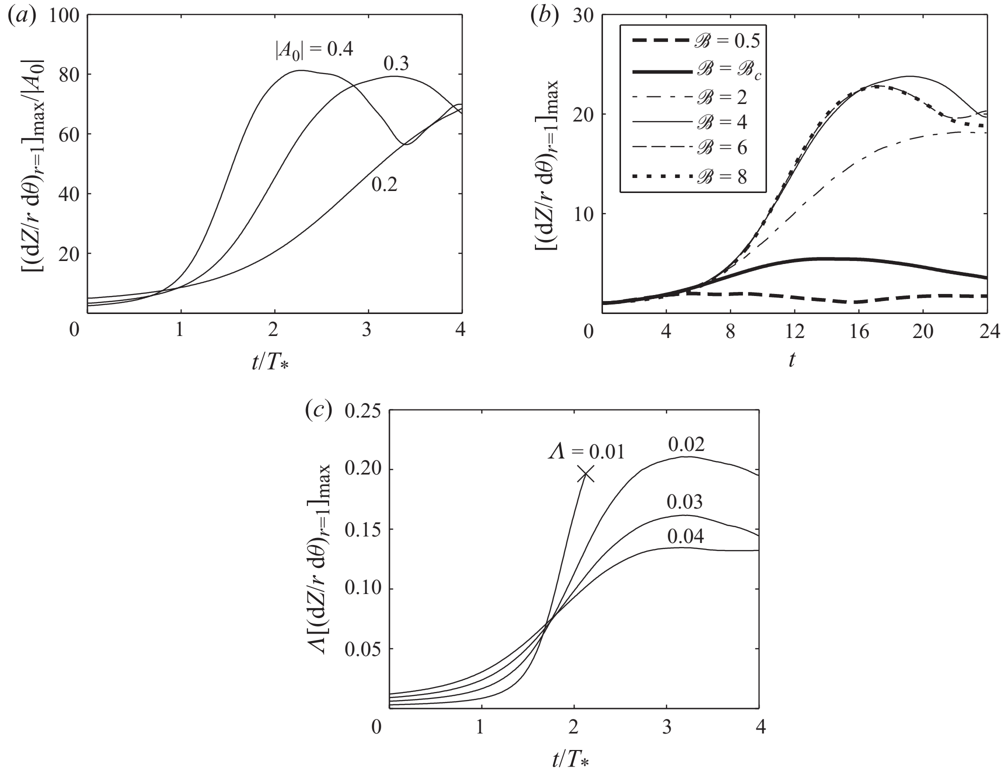

FIGURE 8. Time series of the maximum azimuthal gradient of the isopycnal amplitude Z at $r = 1$ for: (*a*) different amplitudes A_0 with fixed Burger number $\mathscr{B} = 4$ and aspect ratio $\Lambda = 0.025$; (*b*) different Burger numbers with fixed $|A_0| = 0.3$ and $\Lambda = 0.025$; and (*c*) different aspect ratios with fixed $\mathscr{B} = 4$ and $|A_0| = 0.3$.

transverse motions. Steepening of the internal seiche on a non-rotating frame is well documented (e.g. Horn *et al.* 2001, 2002; Boegman, Ivey & Imberger 2005*b*; Sakai & Redekopp 2010).

For larger $\mathscr{B}(>4)$, the steepening rate is very similar. In figure 9, we show snapshots of the Z field at fixed time ($t = 16$) for different values of $\mathscr{B}$ along with their initial conditions. At $t = 16$, the wavefront reached a near maximum slope, and the front had already generated oscillatory waves on its tail. We also observe in the figure that the wavelength of the oscillatory tail becomes shorter for larger $\mathscr{B}$, and the radial width of these waves becomes shorter for larger $\mathscr{B}$ ($l_K \sim c/\mathscr{B}$). Figure 8(*c*) shows the gradient of the wavefront as a function of time for different Λ for fixed $A_0 = -0.3$ and $\mathscr{B} = 4$. In the figure the gradients are all multiplied by their respective $\Lambda (= h_1/r_0)$ to show the actual (non-scaled) values. As seen in (2.19*a*, *b*), Λ^2 scales the dispersive terms. For small Λ, the dispersive effect becomes very small and the evolution model becomes more like a non-dispersive shallow water model where the wavefront evolves to a shock. The rate of steepening becomes greater, and it reaches a larger maximum for smaller Λ. For $\Lambda = 0.01$, the gradient became so steep for the present spectral resolution that the numerical integration was terminated at $t \approx 2$ due to emergence of Gibb's phenomenon. In figure 10 we show snapshots of the Z field at $t = 17.5\,(\approx 3T_*)$ for different values of Λ. It can be seen that the smaller Λ (shallower lake) generates an oscillatory tail of shorter wavelength. An alternative view of the snapshots in

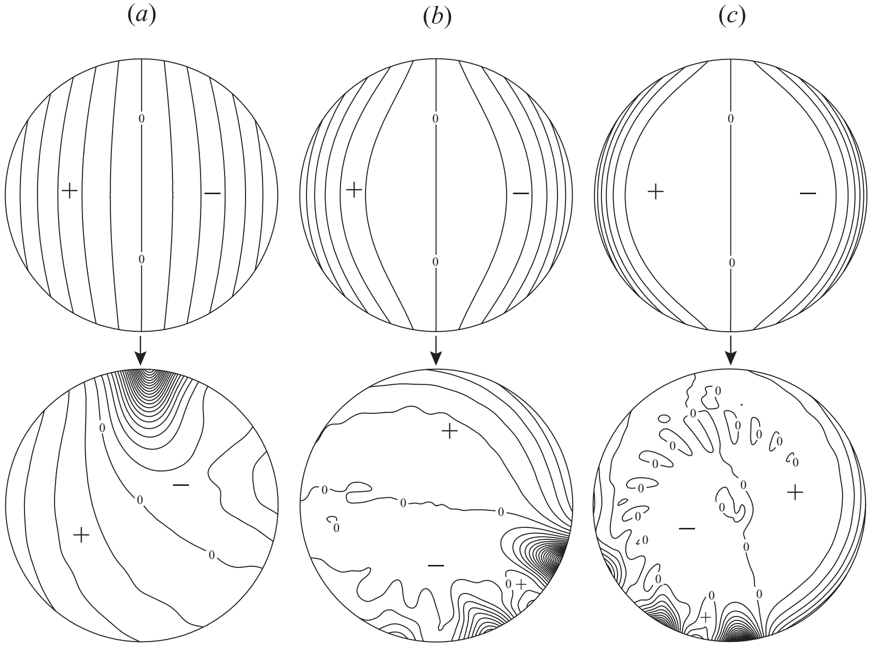

FIGURE 9. Comparison of the isopycnal amplitude Z for different Burger numbers (a) $\mathscr{B}=2$, (b) $\mathscr{B}=4$ and (c) $\mathscr{B}=8$ at $t=0$ (upper row) and $t=16$ (lower row). Contour level step is 0.05.

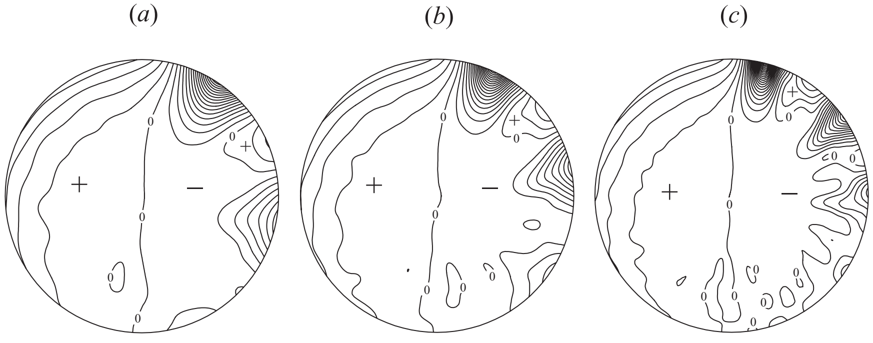

FIGURE 10. Comparison of the isopycnal amplitude Z for different aspect ratios (a) $\Lambda=0.04$, (b) $\Lambda=0.03$ and (c) $\Lambda=0.02$ at $t=17.5$. $\mathscr{B}=4$ and contour level step is 0.05.

figure 10 is obtained by noting that the product of the two dimensionless parameters $\mathscr{B}$ and Λ yields the frequency ratio $f/\mathscr{N}_0$. Hence, the sequence of snapshots in figure 10 correspond to increasing values of the Brunt–Väisälä frequency at fixed latitude and fixed basin size.

Steepening of the wavefront and its subsequent generation of oscillatory waves implies nonlinear energy transfer from basin scale to smaller scales of fluid motion. A spectral method is very advantageous for quantifying the energy contained in each of the discrete wavenumbers. In figure 11 a horizontal wavenumber spectrum is shown of the vertically integrated potential energy at $t=12\,(\approx 2T_*)$ for different amplitudes for $\mathscr{B}=4$ and $\Lambda=0.025$, along with the corresponding snapshots of the Z field. The spectral energy density is normalized by the total potential energy, and the horizontal wavenumber field is a discrete set of Fourier azimuthal modes (m) and radial

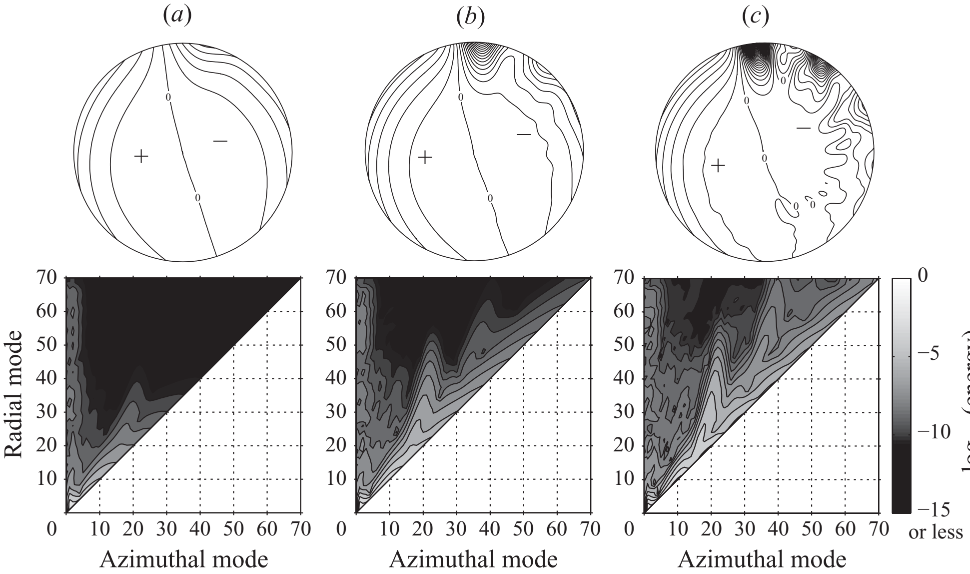

FIGURE 11. Comparison of potential energy spectrum of the Kelvin wave (M1R1+) at $t = 12$ for different initial amplitudes (*a*) $A_0 = -0.2$, (*b*) $A_0 = -0.3$ and (*c*) $A_0 = -0.4$ along with the corresponding isopycnal amplitude Z.

one-sided Jacobi polynomial modes (n) within the spectral truncation $N = 70$. For clarity, the definition of the field energy density is

$$E \equiv \frac{1}{2}\{u^2 + v^2 + w^2\} + \frac{1}{2}\frac{\sigma^2}{\mathscr{N}^2}, \tag{6.2}$$

where the first bracketed term corresponds to kinetic energy and the second corresponds to potential energy. Although the potential energy term is expressed by an infinite series of higher-order terms (e.g. see Gerkema 2003), they are less significant and hence we truncated them in this study. For a single vertical mode and uniform depth, (6.2) is expressed after scaling as

$$E \equiv \frac{1}{2}\left\{(U^2 + V^2)\phi'^2(z) + \Lambda^2\left(\frac{\partial U}{\partial r} + \frac{U}{r} + \frac{1}{r}\frac{\partial V}{\partial \theta}\right)^2 \phi^2(z)\right\} + \frac{1}{2}Z^2\phi^2(z). \tag{6.3}$$

The kinetic energy of the vertical component of velocity can be also neglected noting $w/v \sim \Lambda \ll 1$, but we retained it here. Initially, all the energy is concentrated in azimuthal mode one. In the linear model, the energy is contained in azimuthal mode one at all times, which was confirmed in our numerical code by turning off all the nonlinear terms. For $A_0 = -0.2$, the front is not quite steepened at $t = 12$ and most of the energy is still contained in $m = 1$. For larger amplitudes, the wavefront becomes steeper entailing oscillatory waves, and then more energy is found in higher modes. In figure 12, we present a total energy spectrum as a function of azimuthal mode for several different times for $\mathscr{B} = 4$, $\Lambda = 0.025$ and $A_0 = -0.3$. Spectral convergence is readily observed from the whole energy spectrum (figure 12*a*). Looking at the enlarged plot (figure 12*b*), the energy in higher modes increases in time, and the energy in $m = 1$ decreases in exchange. At $t = 16\,(\approx 2.7T_*)$, a spectral energy peak emerges at $m = 8$, which corresponds to the azimuthal wavenumber of oscillatory waves. At $t = 20\,(\approx 3.4T_*)$, the oscillatory wave gains more energy, being slightly stretched due

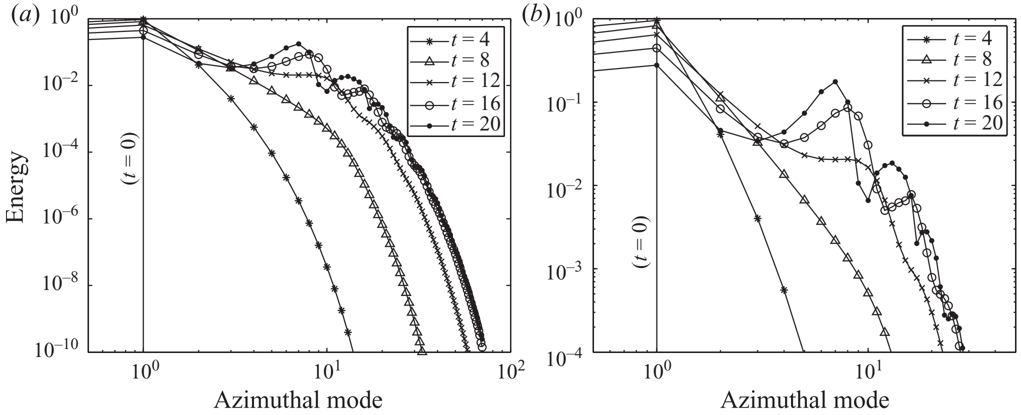

FIGURE 12. (*a*) Azimuthal modal energies of the Kelvin wave (M1R1+) at different times. Energies in lower modes are magnified in (*b*).

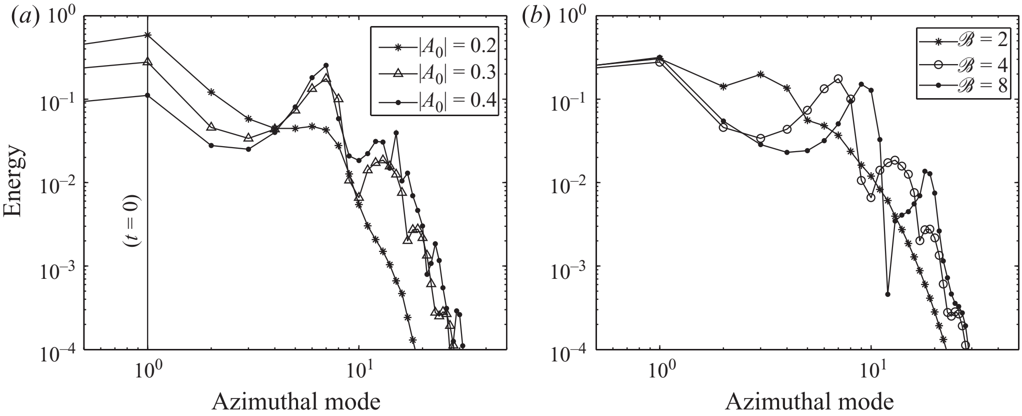

FIGURE 13. Azimuthal modal energies of the Kelvin wave (M1R1+) at $t = 20$ for: (*a*) different initial amplitudes A_0 with fixed Burger number $\mathscr{B} = 4$ and (*b*) different Burger numbers with fixed amplitude $A_0 = -0.3$.

to dispersion. Figure 13(*a*) shows the total energy spectrum at $t = 20$ for different initial amplitudes. Again, more energy is found in higher modes at the expense of energy in $m = 1$ for larger amplitude. For $A_0 = -0.2$ at $t = 20$, the oscillatory tail is still undeveloped, but for larger amplitudes the oscillatory tail is already developed and a spectral energy peak appears at $m = 7$. Figure 13(*b*) shows the similar azimuthal energy spectrum at $t = 20$ for different values of $\mathscr{B}$ for $A_0 = -0.3$. With this amplitude, the oscillatory tail is already developed at $t = 20$. The figure indicates that the spectral energy peak appears in higher azimuthal modes for larger $\mathscr{B}$, which is qualitatively consistent with the observation of figure 9.

Recently, the internal wave evolution in a circular basin of uniform depth was studied in laboratory experiments (Wake, Gula & Ivey 2004, 2005). However, the nonlinear steepening was not observed in their experiments. The vertical structure was a two-layer configuration, and for most of the experimental runs the upper and lower layer depths were set equal. In such a case, the coefficient of the leading nonlinear term $\beta^{(u,v)}$ is identically zero, which can greatly reduce the chance of

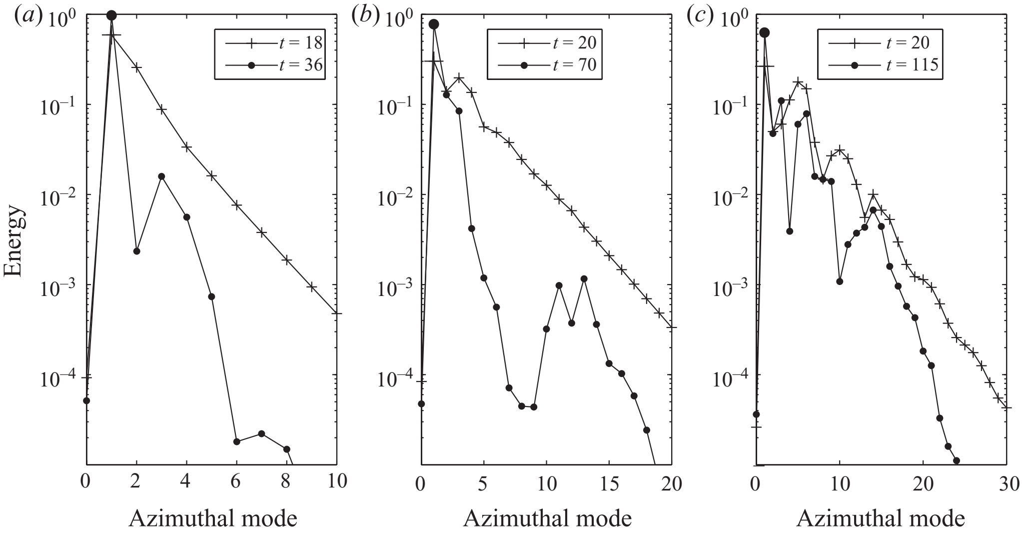

FIGURE 14. Azimuthal modal energies of the Kelvin wave (M1R1+) for (*a*) $\mathscr{B}=\mathscr{B}_c(=\sqrt{2}c)$, (*b*) $\mathscr{B}=2$ and (*c*) $\mathscr{B}=3$. Energy values are normalized by the initial total energy.

observing nonlinear effects. Also, the larger dissipation common in laboratory tanks possibly damps the fluid motion before the nonlinear steepening becomes significant.

Earlier studies of the evolutionary dynamics described by the KdV equation on the periodic interval revealed the phenomenon of recurrence (cf. Zabusky & Kruskal 1965). The weakly nonlinear limit of the problem defined by (2.1), applied to motion in a narrow straight channel when the Rossby radius is small, is also reducible to a KdV equation (Grimshaw 1985; Melville *et al.* 1989) for evolution along the channel. With these facts in view, and noting that the circular lake necessarily involves evolution in a periodic domain (azimuthally), we investigated the potential for reconstruction of the Kelvin wave initial condition for different Burger numbers at fixed initial amplitude, aspect ratio and environmental density structure.

In the circular lake case, where evolution for a single vertical mode occurs in the plane of a disc, energy can flow between both azimuthal and radial modes and the potential for recurrence is fundamentally altered. Nevertheless, there remains a potential for at least a ‘partial’ (i.e. qualitative) recurrence at low Burger numbers where the Kelvin wave dispersion restricts the flow to higher radial modes. In figure 14 we depict in azimuthal wavenumber space the evolution of an M1R1 Kelvin wave initial condition at several Burger numbers. Both the energy spectrum at the time when initial steepening and generation of oscillatory waves occur, plus the corresponding spectrum at a subsequent time when the energy in the lowest azimuthal mode achieves its first maximum (i.e. the earliest form of a ‘reconstruction’ occurs), are shown. At the lowest Burger number chosen ($\mathscr{B}=\mathscr{B}_c=\sqrt{2}c$), the linear dispersion relation allows only the lowest radial mode. At higher Burger numbers, successive radial modes are accessible to the linear system (e.g. see figure 9*c*; the dispersive tail spreads farther into the interior than the primary Kelvin wavefront). It is clear from figure 14 that a near recurrence occurs for the lowest Burger number, but that any semblance of a recurrence is quickly lost due to an apparent irreversible flow of energy to higher radial modes at higher Burger numbers.

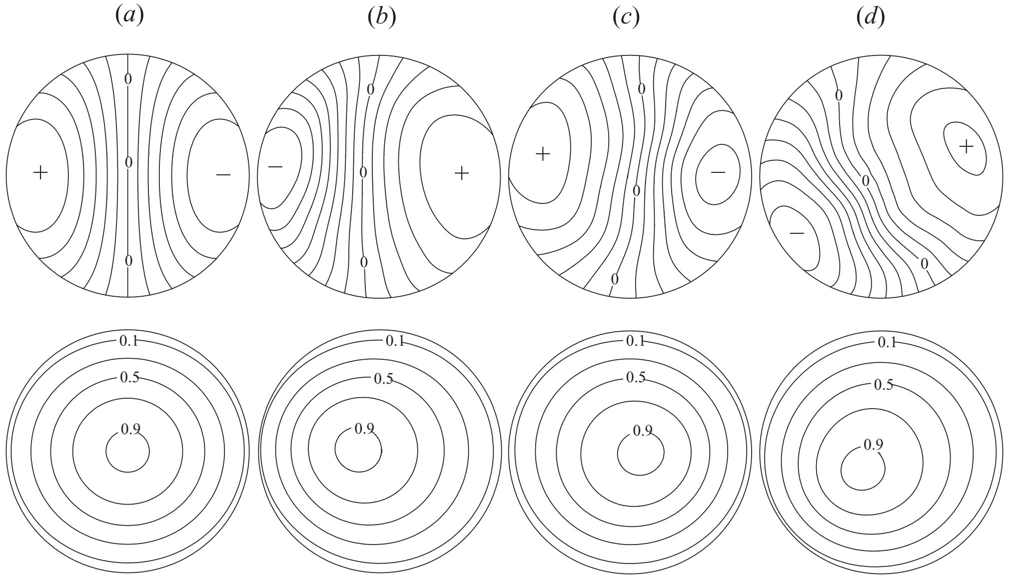

FIGURE 15. Evolution of the Poincaré wave (M1R1–). Snapshots of the isopycnal amplitude Z (upper row) and the magnitude of the velocity amplitude $\sqrt{U^2+V^2}$ (lower row) are taken at (a) $t=0$, (b) $t=0.7$, (c) $t=1.4$ and (d) $t=24$. Contour level step for the isopycnal amplitude is 0.05.

6.2. *Evolution of Poincaré wave on uniform depth*

For the next initial value problem, we choose a Poincaré wave of azimuthal mode one and radial mode one (M1R1–). A typical portrait of Poincaré wave evolution obtained by numerical simulation is shown in figure 15 for $\mathscr{B}=4$, $\Lambda=0.025$ and $A_0=-0.3$. The initial condition is symmetric, but the field quickly loses its symmetry as it evolves. The asymmetric field subsequently tends to return to a near symmetric field, and this repeats aperiodically. If the model is linear hydrostatic, the field is symmetric permanently, rotating in an anti-cyclonic direction with constant speed without changing shape. Contrary to the Kelvin wave, the fluid velocity is the largest at $r=0$ for Poincaré waves. Looking at the lower row of figure 15, contours of the magnitude of the velocity are symmetric having their maximum at $r=0$ initially, but the velocity contours become eccentric having their maximum off the basin centre as the wave evolves. It can be also observed from the figure that the isopycnal amplitude is larger on the side where the maximum velocity is found. This asymmetric modulation of wave amplitude persists for the rest of the evolution (see $t=24\approx 17.5T_*$ in figure 15), and there is no sign of the wavefront steepening which was observed in Kelvin wave evolutions studied earlier in this section. Although the result is not shown here, we simulated this case with much smaller Λ $(=0.001)$, but both results were indistinguishable. This is because the non-hydrostatic term is effective only when the field gradient is large, which is not the case for the Poincaré wave evolution. In figure 16, we plot the maximum and minimum values of Z as functions of time for different initial amplitudes. The amplitude modulation is aperiodic and biased asymmetrically on the negative side, and the amount of modulation becomes larger for a larger initial amplitude.

Figure 17(a, b) shows the normalized potential energy spectrum of the field at $t=4\approx 3T_*$ for different amplitudes, along with snapshots of the Z field. Although

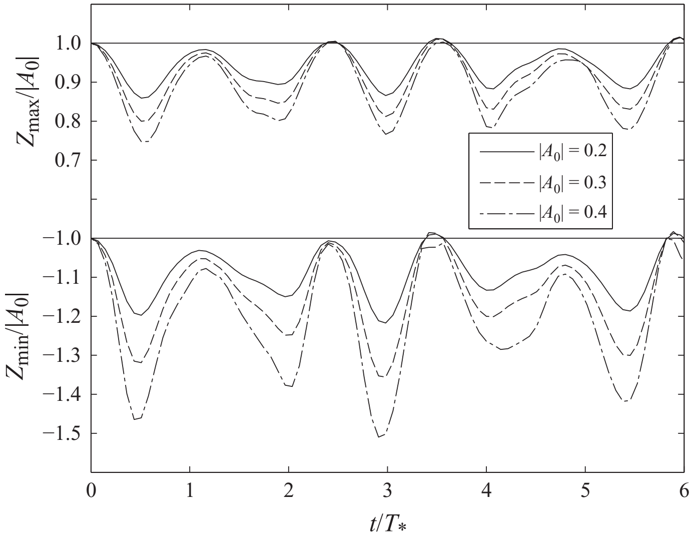

FIGURE 16. Time series of the minimum and the maximum values of the isopycnal amplitude Z for Poincaré waves (M1R1−) of different amplitudes.

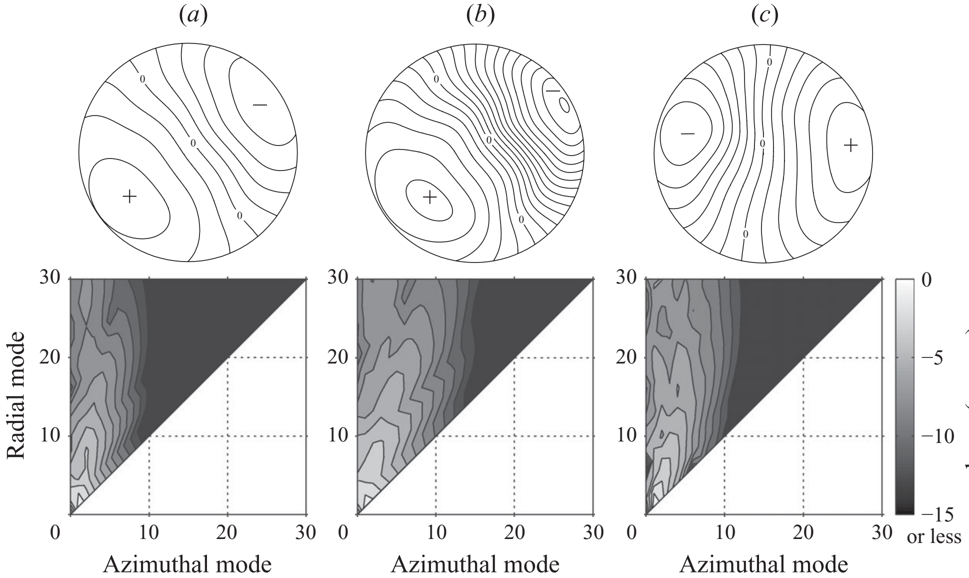

FIGURE 17. Comparison of potential energy spectrum of the Poincaré wave (M1R1–) for different initial amplitudes (*a*) $A_0 = -0.2$ and (*b*) $A_0 = -0.4$ at $t = 4$ and (*c*) $A_0 = -0.3$ at later time $t = 20$ along with the corresponding isopycnal amplitude Z.

the actual spectral resolution is $N = 70$, the energy spectrum is truncated to $N = 30$ because of insignificant energy in higher modes. Energy is concentrated in $m = 1$, and it spreads over higher radial modes rather than higher azimuthal modes, implying faster spectral convergence in azimuthal modes. More energy spreads over higher radial and azimuthal modes for larger initial amplitude ($A_0 = -0.4$), and the field becomes more asymmetric. In figure 17(*c*), we also show the case at $t = 20 \approx 14.5T_*$

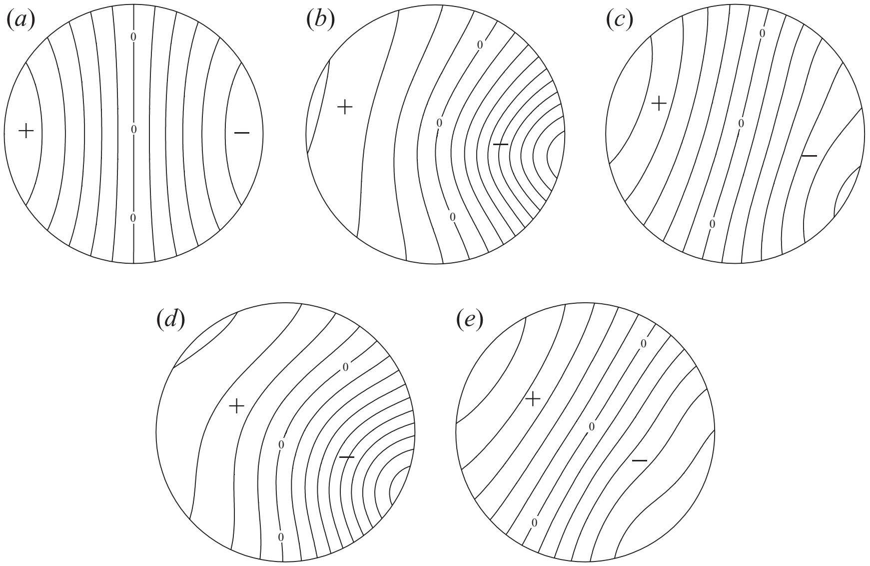

FIGURE 18. Pseudo recurrence of a Poincaré-type wave (M1R1+ with the Burger number $\mathscr{B} = 1/2$). Snapshots of the isopycnal amplitude Z are taken at (*a*) $t = 0$, (*b*) $t = 8(1.97T_*)$, (*c*) $t = 16(3.93T_*)$, (*d*) $t = 24(5.9T_*)$ and (*e*) $t = 32(7.86T_*)$. Contour level step is 0.05.

for $A_0 = -0.3$ to indicate that a similar modal energy structure persists even after a long time.

The amplitude modulation is also observed for cyclonic superinertial wave modes (Poincaré type). Figure 18 shows evolution of the isopycnal amplitude starting with the M1R1+ initial condition for $\mathscr{B} = 1/2\,(<\mathscr{B}_c)$. The field is symmetric initially, but the amplitude in the negative side increases and the amplitude in the positive side decreases ($t = 8 \approx 2T_*$) as the wave evolves. Later, the asymmetry returns very nearly to the symmetry of the initial condition ($t = 16 \approx 4T_*$), and this is repeated approximately every $4T_*$. The recurrence of the initial condition has been found in the integrable KdV model under periodic boundary conditions (Zabusky & Kruskal 1965). The KdV evolution involves steepening and generation of solitary waves which have amplitude-dependent phase speeds. The recurrence is achieved when all the soliton's phases become very close. However, the pseudo recurrence character found in the Poincaré wave presented above is of a different type because of the absence of front steepening and subsequent generation of solitary-like waves.

For Kelvin waves, fluid advection is confined near the boundary and the velocity vectors are oriented in the propagation direction. Hence, the steepening of the wavefront can be directly driven by this 'obstacle-free' alongshore current similar to one-dimensional (non-rotating) progressive waves. For Poincaré waves, on the other hand, basin-scale fluid advection is pronounced at the centre of the basin, and the velocity vectors are perpendicular to both the boundary and the wave propagating direction (i.e. the field advection and the wave vector are 'out-of-phase'). It is conjectured that such an out-of-phase feature of the Poincaré eigenstructure possibly impedes the progressive nonlinear steepening of the dominant flow, and that nonlinearly-accelerated flow bounces within the confined basin, breaking the symmetry of the flow structure that is oscillatory in time.

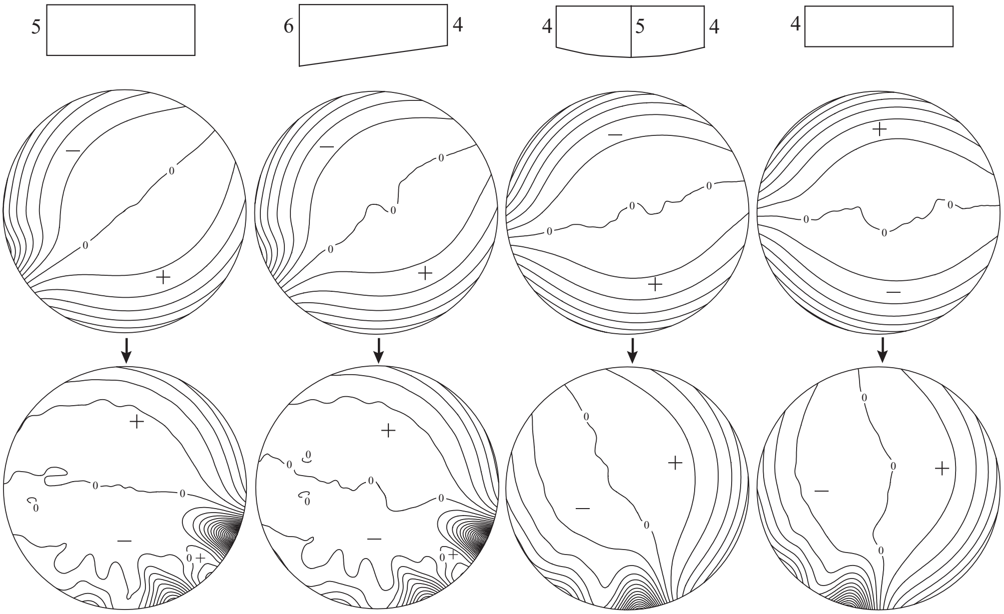

FIGURE 19. Snapshots of the isopycnal amplitudes Z of the Kelvin waves at $t = 8$ (upper contour panels) and at $t = 16$ (lower contour panels) for different depth profiles. The depth profiles are depicted on the top of each column.

6.3. *Evolution on variable depth*

We now briefly examine the effects of variable depth. We fix the metalimnion depth at the value used in the previous section ($h_2 = 1$), and perturb the depth of the hypolimnion from the base depth $h_3 = 3$. We consider two simple model topography profiles: (i) a slanted bottom surface

$$h_b = 1 + h_2 + h_3 + \Delta h r \cos\theta, \tag{6.4}$$

and (ii) a symmetric parabolic bottom surface

$$h_b = 1 + h_2 + h_3 - \Delta h r^2, \tag{6.5}$$

where Δh is in each case a depth perturbation scaled by h_1. These depth functions are regular at $r = 0$. Vertical structure profile (5.1), which is independent of h_3, holds over the whole domain.

We first consider evolution of Kelvin waves in an environment described by (6.4) and (6.5). In figure 19, snapshots of isopycnal amplitude at two different times are tabulated for a slanted bottom with $\Delta h = 1$ and a parabolic bottom with $\Delta h = 1$. Included in figure 19 are results for constant depth cases $h_3 = 3$ and $h_3 = 2$ for comparison. The Burger number and the aspect ratio were set at $\mathscr{B} = 4$ and $\Lambda = 0.025$, respectively, and resolution of the numerical integration was set with $N = 70$ and $\Delta t = 0.0025$. For all the cases in the figure, the system was integrated from the common initial condition, which is a linear hydrostatic Kelvin wave solution for $h_3 = 3$ (uniform depth) with the initial amplitude $A_0 = -0.3$ (see figure 5 at $t = 0$). The field evolution for the slanted basin appears nearly the same as the original case of constant depth. However, the parabolic basin exhibits a slower phase speed and slower steepening than the original flat basin. The evolution in the parabolic basin rather resembles the one for the constant depth case $h_3 = 2$, the same depth as at the basin perimeter in the parabolic

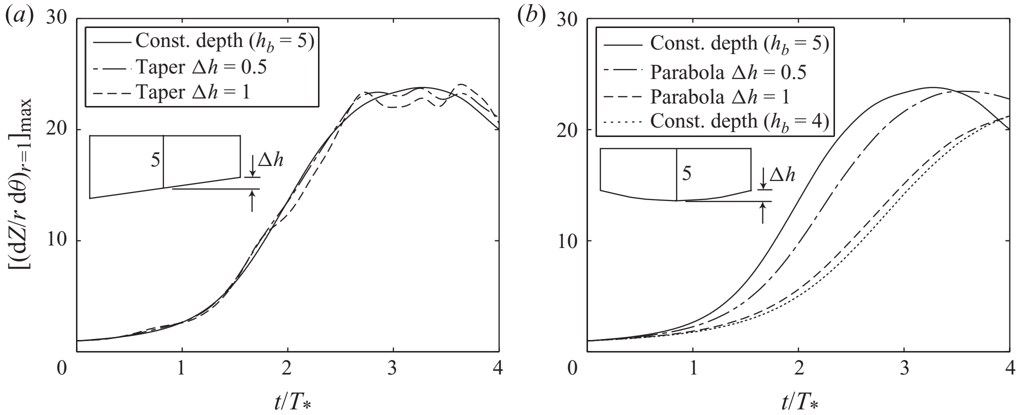

FIGURE 20. Time series of the maximum azimuthal gradient of the isopycnal amplitude Z at $r = 1$ for (a) slanted depth profile and (b) parabolic depth profile. The time t is scaled by T_*, the linear Kelvin wave period with a constant depth ($h_b = 5$).

basin. The slow phase speed primarily resulted from the fact that the linear phase speed is smaller for shallower depth (i.e. $c = 0.9395$ at $h_3 = 3$ and $c = 0.8763$ at $h_3 = 2$, and note that the wave frequency is scaled by c for given $\mathscr{B}$ as implied in figure 1).

Figure 20 shows the maximum azimuthal slope of the isopycnal amplitude at the basin perimeter as a function of time for different values of depth perturbation in both the slanted and parabolic basin configurations. For the slanted basin, the slope fluctuates as the wave travels over the variable depth cyclonically. The fluctuation becomes greater for larger depth perturbation, but it is not relatively significant for the present amount of perturbation. On the contrary, the rate of steepening is significantly affected by the depth at the basin perimeter in the parabolic basin. In the same figure, it can be seen that the rate of steepening for $\Delta h = 1$ and the uniform depth of $h_b = 4$ for the parabolic basin are very similar. Similar to the phase speed argument above, the coefficients of primary nonlinear terms in (2.19a, b) are $\beta^{(u,v)} = -0.3691$ at $h_3 = 3$ and $\beta^{(u,v)} = -0.2594$ at $h_2 = 2$, implying less nonlinearity for smaller depth, and consequent slower growth of the wavefront near the basin perimeter where much of field kinetic energy is confined. For the slanted basin, the environmental coefficients vary sinusoidally centred at values at average depth along with the perimeter. This is why similar evolution pictures to those of the original flat basin appear in the case of the slanted basin.

The field evolution of the lowest Poincaré waves (M1R1–) in basins of variable depth established above is considered for the rest of this section. Both physical and numerical parameter configurations are the same as those for the Kelvin wave case noted above, although the Poincaré wave simulation requires less numerical resolution due to lack of progressive front steepening. Figure 21 shows snapshots of the isopycnal amplitude at different times for the slanted basin of $\Delta h = 1$, along with those for the original flat basin. These snapshots are selected in such a way that either the negative side of Z shoals ($t = 2.7$ and $t = 4.1$) or the positive side of Z shoals ($t = 3.4$). Although the wave phases are nearly the same for the slanted and flat basin, their amplitudes are different. We also present on the third column in figure 21 the normalized difference of isopycnal amplitudes between those of the slanted (Z_2) and flat basin (Z_1), i.e. $(Z_2 - Z_1)/|A_0|$. It can be seen from the figure that the amplitude

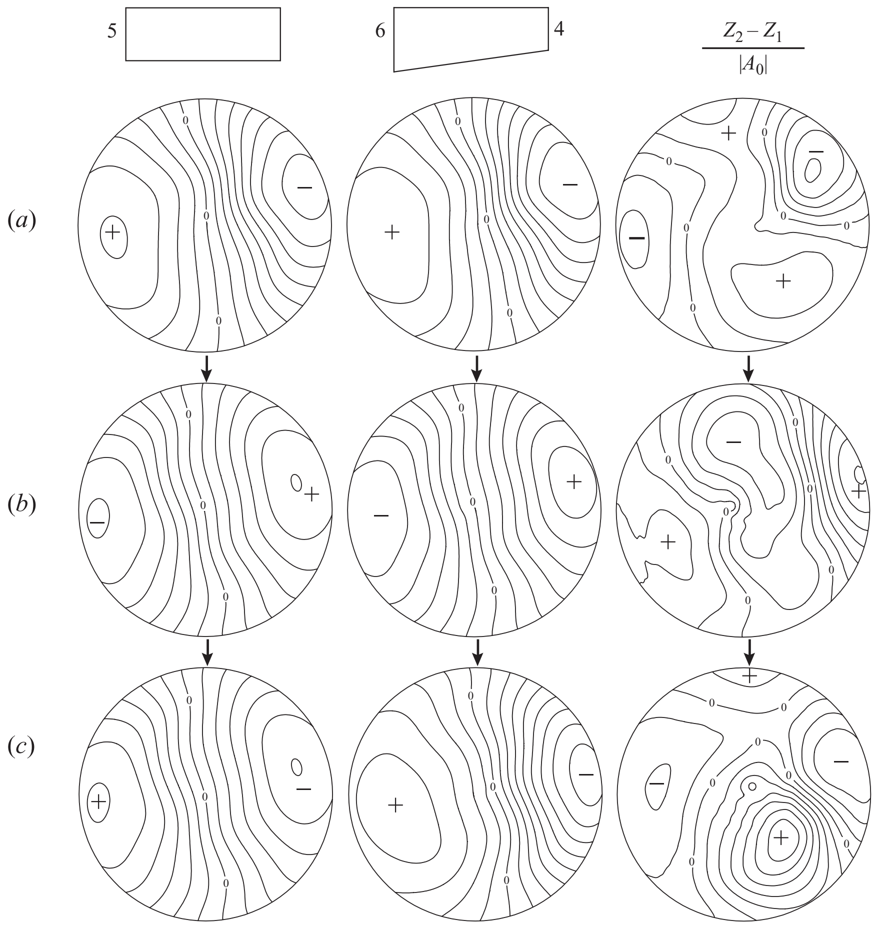

FIGURE 21. Comparison of the isopycnal amplitudes for the uniform depth case (Z_1) and the slanted depth case (Z_2) at (*a*) $t = 2.7\,(1.96T_*)$, (*b*) $t = 3.4\,(2.47T_*)$ and (*c*) $t = 4.1\,(2.98T_*)$, where T_* is the period of the linear Kelvin wave with a constant depth $h_3 = 3$ (case *a*). The contour level step for these plots is set to be 0.05. On the right-hand column the difference of Z_1 and Z_2 scaled by the initial amplitude $|A_0|$ is plotted with a contour level step 0.02.

of the wave increases as the wave shoals, and the amplitude decreases as the wave travels into the deep side of the basin.

We measured the maximum and minimum values of Z as functions of time for the slanted and flat basin and plotted the values in figure 22. The figure implies that the nonlinear amplitude modulation is dominant over the modulation induced by the variable depth. The modulation of amplitude for variable depth is about 10 % of the original amplitude (see also the case for the linear variable depth model in figure 22), but the nonlinear modulation corresponds to 35 %. In contrast to Kelvin waves, the kinetic energy density is concentrated at the basin centre in Poincaré wave fields. Hence, it is naturally expected that the depth change confined toward the basin perimeter affects Poincaré field evolution only slightly. To demonstrate this, a time series of the extremal values of the isopycnal amplitude for the parabolic basin with $\Delta h = 1$ are also included in figure 22. It is evident from the figure that the extremal values obtained in the parabolic basin are close to those obtained in the flat basin.

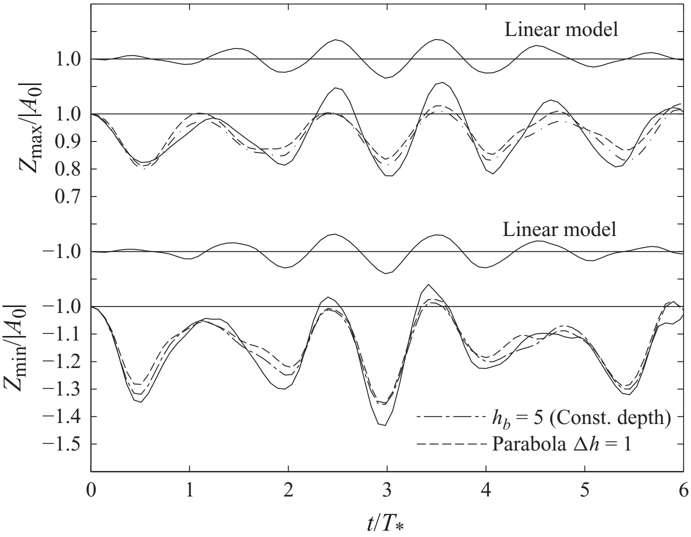

FIGURE 22. Time series of the maximum and the minimum values of the isopycnal amplitude Z of the Poincaré wave over the slanted depth profile with $\Delta h = 1$. For comparison time series for the linear hydrostatic model and for different depth cases are also included in the figure. The time t is scaled by T_*, the period of the linear Poincaré wave with a constant depth ($h_b = 5$).

7. Wind-forced evolution

We apply our evolution model to the wind-forced problem, where multiple horizontal wave modes can be excited and they coexist with, or may even generate, other modes via nonlinear interaction. We limit our study to a lake of uniform depth which is subject to wind-forcing of finite duration. Uniform wind stress over the basin surface is ideal as a fundamental model, but it is not suited to the spectral model due to the fact that such a stress function is discontinuous at the basin perimeter, which can immediately destroy the spectral convergence of numerical solutions. Instead, we use a radially symmetric stress directed along the x(horizontal)-axis written by a simple formula

$$\boldsymbol{\tau}_h = \frac{n_s + 1}{n_s}(1 - r^{2n_s})\{1 - u_s(t - t_0)\}\boldsymbol{e}_x, \tag{7.1}$$

where $u_s(t)$ is the Heaviside step function, t_0 is wind-forcing duration and $\boldsymbol{e}_x = \cos\theta\boldsymbol{e}_r - \sin\theta\boldsymbol{e}_\theta$. This stress starts from a maximum value at the basin centre and decreases to zero toward the perimeter. The average of the stress over the surface is unity, and the magnitude of the stress is controlled by the Wedderburn number $\mathscr{W}$. The parameter n_s in (7.1) is an integer parameter to control the stress shape: $n_s = 1$ gives a parabolic distribution, and increasing n_s decreases the stress at the basin centre while increasing the stress near the perimeter making the distribution close to uniform ($|\boldsymbol{\tau}_h| \to 1$ as $n_s \to \infty$). It is clear from (7.1) that the wind energy is injected only through azimuthal mode one. It is also important to note that (7.1) is a regular function at $r = 0$. The wind-forcing duration t_0 is parameterized by a fraction κ_w of the inertial period T_i, i.e.

$$t_0 = \kappa_w T_i = \kappa_w \frac{2\pi}{\mathscr{B}}. \tag{7.2}$$

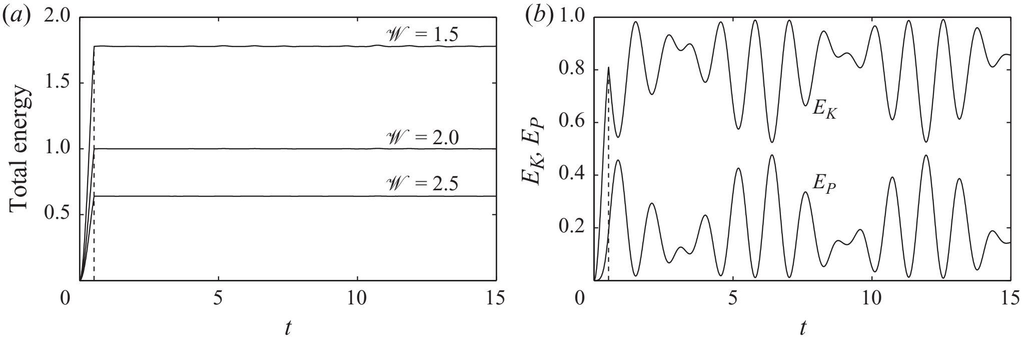

FIGURE 23. (*a*) Time series of the total energy for different Wedderburn numbers $\mathscr{W}$ and (*b*) time series of kinetic (E_K) and potential (E_P) energies for $\mathscr{W} = 2$.

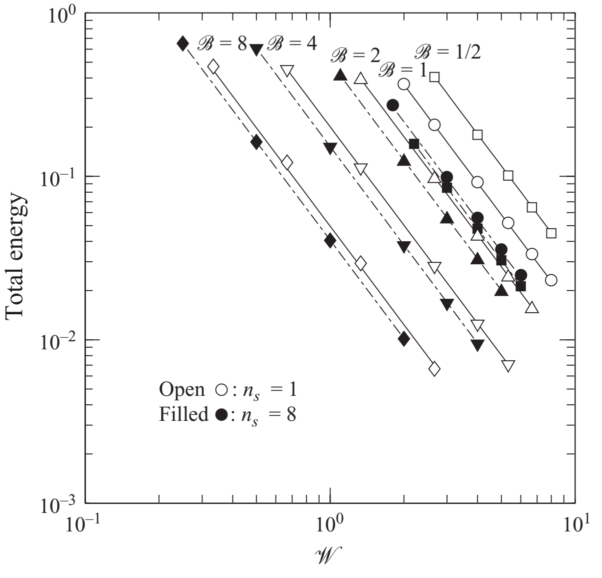

FIGURE 24. Total energy as a function of the Wedderburn number $\mathscr{W}$.

Physical and numerical parameters are set to $h_b = 5$ ($h_2 = h_1 = 1$ and $h_3 = 3$), $\Lambda = 0.001$, $N = 31$ and $\Delta t = 0.005$, unless otherwise noted.

We computed the volume integral of the total energy density as a function of time for different Wedderburn numbers for $\mathscr{B} = 4$, $n_s = 1$ and $t_0 = T_i/3$, and show results in figure 23(*a*). The field energy increases until the wind is turned off, and the energy then stays approximately constant for the rest of the evolution due to the absence of friction damping in the model. The total energy is not necessarily an exact constant, however, because we used the truncated expression (6.3). Figure 24 shows the total energy at $t = t_0$ as a function of the Wedderburn number for different values of $\mathscr{B}$ and n_s. The total energy is proportional to $\mathscr{W}^{-2}$ regardless of the stress shape and Burger number. We also show in figure 23(*b*) the integral of kinetic energy (E_K) and potential energy (E_P) over the basin volume as functions of time for $\mathscr{W} = 2$. Oscillatory energy exchange between E_P and E_K is clearly observed, which readily suggests that multiple wave modes coexist in the wind excited field. For a specific wave mode in the linear

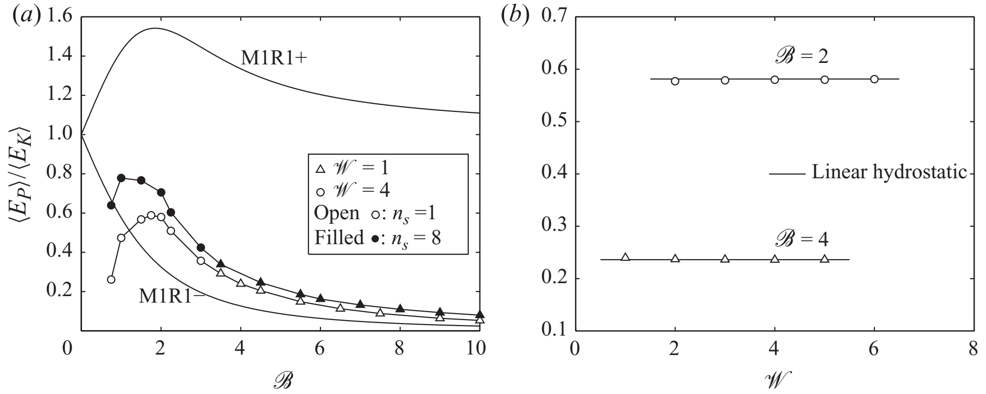

FIGURE 25. (*a*) Energy ratio as a function of Burger number $\mathscr{B}$ for different wind stress profiles and (*b*) energy ratio as a function of the Wedderburn number $\mathscr{W}$ for different Burger numbers.

hydrostatic model, one can easily show from (3.2) that E_P and E_K are independent of time for a given amplitude (a wave of permanent form and frequency rotates around a basin centre). If multiple wave modes coexist in the wave field an energy exchange between E_P and E_K can occur, primarily because frequencies of all the wave modes are distinct. Hence, in a real wave field, computing energy partitioning between E_P and E_K is meaningful only in a time average sense.

In figure 25(*a*), we show the energy partition between E_P and E_K as a function of Burger number for $t_0 = T_i/3$. Each energy is averaged in an interval of the longest wave period for the given Burger number (i.e. Kelvin wave period), after the wind is turned off. The computed energy partition ranges within ±10 % compared to the value averaged in three Kelvin wave periods. We also include in the figure the energy ratio for linear hydrostatic Kelvin (M1R1+) and the gravest Poincaré (M1R1−) waves. Energy partition shows a preference for kinetic energy for the Poincaré wave mode, especially for larger $\mathscr{B}$. In figure 25(*b*), we also show the energy partition as a function of Wedderburn number for different Burger numbers, along with the value obtained from the linear hydrostatic model. It can be seen from the figure that the dependence of Wedderburn number on the energy partition is very weak. This suggests that the linear hydrostatic model can serve as a good tool for estimating energetics, at least in the initial stage of free evolution. Wind-forced response of a linear hydrostatic, circular basin has been well documented (Csanady 1968, 1972; Stocker & Imberger 2003). Referring to these works, an analytical solution to the linear hydrostatic model subject to uniform wind stress can be obtained by a Laplace transform approach, and the final result is written in terms of our scaled variables as:

$$\left.\begin{aligned} U &= \frac{k_s}{\mathscr{W}} \sum_{n=1}^{\infty} \frac{A_n}{\mathscr{B}\left(1-\omega_{1n}^2\right)} \left\{ \omega_{1n} \mathscr{R}'_{1n}(r) - \frac{\mathscr{R}_{1n}(r)}{r} \right\} \cos(\theta - \mathscr{B}\omega_{1n} t + \Delta_0), \\ V &= \frac{k_s}{\mathscr{W}} \sum_{n=1}^{\infty} \frac{A_n}{\mathscr{B}\left(1-\omega_{1n}^2\right)} \left\{ \mathscr{R}'_{1n}(r) - \omega_{1n} \frac{\mathscr{R}_{1n}(r)}{r} \right\} \sin(\theta - \mathscr{B}\omega_{1n} t + \Delta_0), \\ Z &= \frac{k_s}{c^2 \mathscr{W}} \sum_{n=1}^{\infty} A_n \mathscr{R}_{1n}(r) \sin(\theta - \mathscr{B}\omega_{1n} t + \Delta_0), \end{aligned}\right\} \qquad (7.3)$$

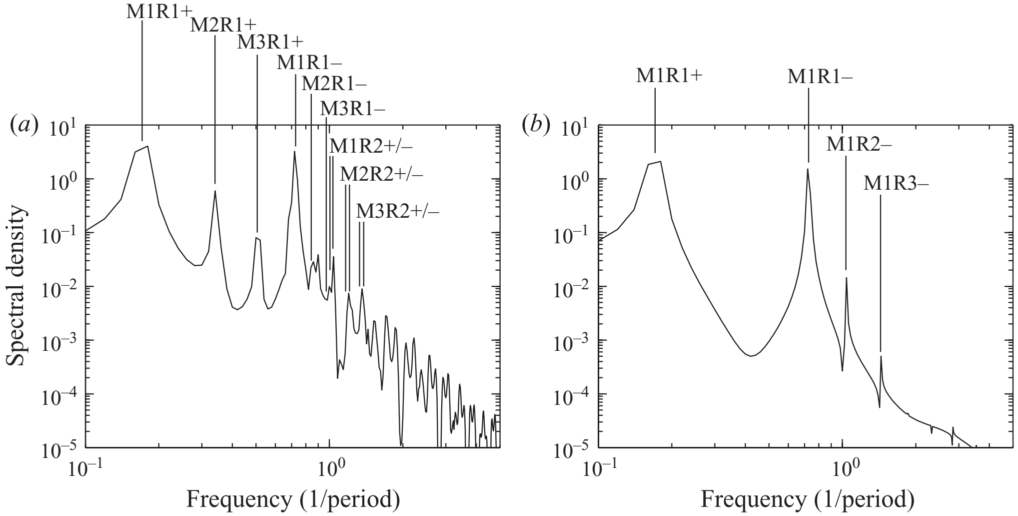

FIGURE 26. Frequency power spectrum of the isopycnal amplitude Z sampled at $(r, \theta) = (1, 0)$ for (a) nonlinear, non-hydrostatic model and (b) linear hydrostatic model.

where $\mathscr{R}_{1n}$ is a normalized modal eigenfunction of azimuthal mode one and nth radial mode with corresponding eigenfrequency ω_{1n}, phase shift $\Delta_0 = \mathscr{B}\omega_{1n}t_0/2$, and A_n is a radial modal amplitude given by

$$A_n = 2\frac{\omega_{1n} - 1}{1 + \omega_{1n} - (\mathscr{B}/c)^2\omega_{1n}^3} \sin\left(\frac{\mathscr{B}\omega_{1n}t_0}{2}\right) \frac{|\mathscr{R}_{1n}^*(r)|_{\max}}{\mathscr{R}_{1n}^*(1)}. \tag{7.4}$$

Note that (7.3) is a solution for post wind-forcing ($t \geqslant t_0$), hence the geostrophic (steady) solution is cancelled in the expression. From (7.3), all field variables are proportional to $k_s \mathscr{W}^{-1}$. This implies that the total energy is proportional to $\mathscr{W}^{-2}$, which is consistent with our numerical result presented in figure 24.

The field response for the linear hydrostatic basin subject to uniform wind stress is constructed by an infinite family of radial modes for azimuthal mode-one waves. Equation (7.4) implies that the magnitude of each modal amplitude ranges from zero to its maximum value every $T_i/2\omega_{1n}$. It can be shown through use of (7.4) that unless the wind blows for too long ($t_0 < T_i$), the dominant wave modes are a Kelvin wave (M1R1+) having the largest amplitude and the gravest Poincaré wave (M1R1−). Once initiated by the wind-forcing, these modal amplitudes are invariant for the rest of the response. In a nonlinear counterpart, although the wind energy is introduced only via azimuthal mode one, the energy can spread over other azimuthal and radial modes via nonlinear interaction. In figure 26(a), we show a frequency power spectrum of the isopycnal amplitude sampled at $(r, \theta) = (1, 0)$ for $\mathscr{B} = 4$ and $\mathscr{W} = 3.5$. The sampling interval is $0 \leqslant t \leqslant 50$, which corresponds to eight and one-half Kelvin wave periods. At this Wedderburn number, the isopycnal amplitude is relatively small (~ 0.12), and the steepening of the Kelvin wave becomes noticeable only after about $t = 40$. We did not sample the signal beyond $t = 50$ due to insufficient numerical resolution to resolve the steepened front. In the figure, frequencies of the first three azimuthal and the first two radial wave modes determined from the linear hydrostatic model are indicated. The spectral peaks agree with these frequencies very well. The Kelvin wave and the gravest Poincaré modes are still dominant modes even in the long time interval. A similar trend was also found for different Burger numbers and sampling points, although these results are not shown here. We also simulated the same case under the linear hydrostatic configuration having all nonlinear and non-hydrostatic terms turned off in our numerical code. The corresponding frequency spectrum is shown in figure 26(*b*). The spectral density has peaks at only azimuthal mode-one waves, which implies there is no energy leakage to other azimuthal modes in the numerical code.

Unless a model is linear hydrostatic, it is not a straightforward task to determine the energy contained in a given wave mode. Motivated by the above results that the Kelvin and gravest Poincaré modes are dominant, we address the energy partition between these dominant modes. In a linear hydrostatic sense, we try to estimate roughly the energy partition from our results obtained by numerical simulation. Assuming the post wind-forcing field is dominated by two wave modes, we write the field solution as a linear superposition of the modes

$$\left.\begin{aligned} U &= \sum_{n=1}^{2} A_n \mathscr{P}_n(r)\cos(\theta - \mathscr{B}\omega_n t - \delta_n),\\ V &= \sum_{n=1}^{2} A_n \mathscr{Q}_n(r)\sin(\theta - \mathscr{B}\omega_n t - \delta_n),\\ Z &= \sum_{n=1}^{2} A_n \mathscr{R}_n(r)\sin(\theta - \mathscr{B}\omega_n t - \delta_n), \end{aligned}\right\} \tag{7.5}$$

where indices $n = 1$ and $n = 2$ represent the Kelvin wave and Poincaré wave mode, respectively. Radial structure functions of the velocities $\mathscr{P}_n(r)$ and $\mathscr{Q}_n(r)$ are defined after (3.2) with $m = 1$, so that

$$\left.\begin{aligned} \mathscr{P}_n(r) &= -\frac{c^2}{\mathscr{B}(1-\omega_n^2)}\left\{\frac{\mathscr{R}_n(r)}{r} - \omega_n \mathscr{R}_n'(r)\right\},\\ \mathscr{Q}_n(r) &= \frac{c^2}{\mathscr{B}(1-\omega_n^2)}\left\{\omega_n\frac{\mathscr{R}_n(r)}{r} - \mathscr{R}_n'(r)\right\}. \end{aligned}\right\} \tag{7.6}$$

The volume integral of the potential energy is computed as

$$\begin{aligned} E_P &= \frac{1}{2}\int_{-H}^{0}\int_{0}^{2\pi}\int_{0}^{1} \mathscr{N}^2(z)\phi^2(z)Z^2(r,\theta,t) r\,\mathrm{d}r\,\mathrm{d}\theta\,\mathrm{d}z \\ &= \frac{\pi}{2} I \left\{ A_1^2 \int_0^1 \mathscr{R}_1^2 r\,\mathrm{d}r + A_2^2 \int_0^1 \mathscr{R}_2^2 r\,\mathrm{d}r \right. \\ &\qquad \left. + 2A_1A_2\cos(\mathscr{B}(\omega_2-\omega_1)t + \delta_2 - \delta_1)\int_0^1 \mathscr{R}_1\mathscr{R}_2 r\,\mathrm{d}r \right\}. \end{aligned} \tag{7.7}$$

The last term in (7.7) is a time fluctuating part of the E_P owing to distinct frequencies of the wave modes. Looking at figure 23(*b*), the primary period of the energy oscillation is measured to be 1.2. Using eigenfrequencies for Kelvin ($\omega_1 = 0.268$) and Poincaré ($\omega_2 = -1.14$) modes for $\mathscr{B} = 4$, the oscillation period is computed to be 1.12, which is close to the measured value. Figure 23(*b*) shows a modulation of the amplitude of the energy oscillation, possibly to contributions from higher wave modes that are not accounted in this two-mode truncation. Taking the time average

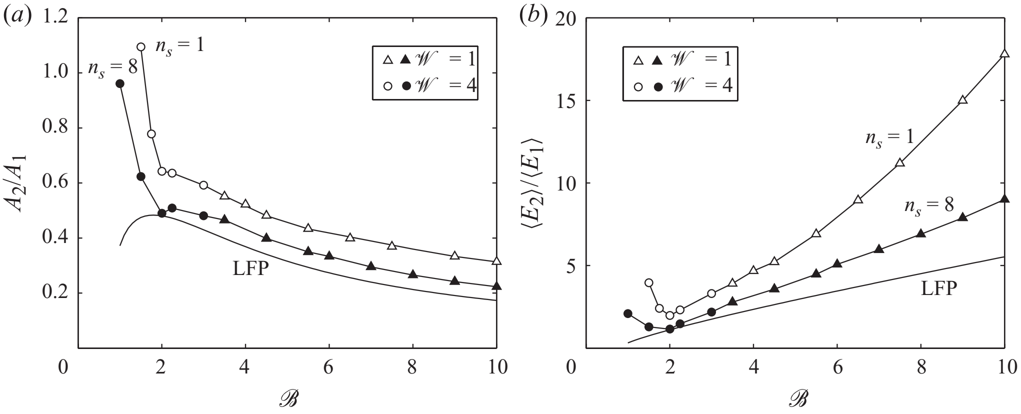

FIGURE 27. (*a*) Estimated amplitude ratio and (*b*) corresponding energy ratio between the Kelvin wave and the Poincaré wave modes as a function of the Burger number $\mathscr{B}$. (LFP = linear forced problem).

of (7.7), the energy fluctuation term vanishes leaving

$$\langle E_P\rangle = \frac{\pi}{2} I \left\{ A_1^2 \int_0^1 \mathscr{R}_1^2 r \,\mathrm{d}r + A_2^2 \int_0^1 \mathscr{R}_2^2 r \,\mathrm{d}r \right\}. \tag{7.8}$$

Carrying out the same procedure for the kinetic energy counterpart yields

$$\langle E_K\rangle = \frac{\pi}{2} \frac{I}{c^2} \left\{ A_1^2 \int_0^1 \left(\mathscr{P}_1^2 + \mathscr{Q}_2^2\right) r \,\mathrm{d}r + A_2^2 \int_0^1 \left(\mathscr{P}_2^2 + \mathscr{Q}_2^2\right) r \,\mathrm{d}r \right\}. \tag{7.9}$$

From (7.8) and (7.9), solving for A_1^2 and A_2^2 yields the amplitude ratio

$$\frac{A_2}{A_1} = \sqrt{\frac{-\gamma\mu_1 + \sigma_1}{\gamma\mu_2 - \sigma_2}}, \tag{7.10}$$

where γ is a ratio of potential to kinetic energy, and σ_n and μ_n are the radial modal energy densities of potential and kinetic energy:

$$\gamma = \frac{\langle E_P\rangle}{\langle E_K\rangle}, \quad \sigma_n = \frac{\pi}{2} I \int_0^1 \mathscr{R}_n^2 r \,\mathrm{d}r \quad \text{and} \quad \mu_n = \frac{\pi}{2}\frac{I}{c^2} \int_0^1 \left(\mathscr{P}_n^2 + \mathscr{Q}_n^2\right) r \,\mathrm{d}r. \tag{7.11}$$

The quantity γ is readily estimated from numerical simulation, and σ_n and μ_n are also readily computed using the eigenfunctions. After computing the amplitude ratio by (7.10), the modal energy ratio $\langle E_2\rangle/\langle E_1\rangle$ is computed

$$\frac{\langle E_2\rangle}{\langle E_1\rangle} = \frac{\sigma_2 + \mu_2}{\sigma_1 + \mu_1} \left(\frac{A_2}{A_1}\right)^2. \tag{7.12}$$

The amplitude and energy ratios of Kelvin and Poincaré waves as functions of $\mathscr{B}$, after using the potential to kinetic energy ratio estimated previously in figure 25(*a*), are shown in figure 27. Corresponding results for the linear forced problem (LFP) described by (7.3) and (7.4) are included in figure 27. For larger n_s (wind stress approaches a uniform distribution), the amplitude as well as energy ratios get close to those of LFP. However, the amplitude ratio deviates substantially from that of LFP for smaller $\mathscr{B}$. Contrary to the uniform wind, the curl of a non-uniform stress (our case) does not vanish, and a non-zero curl of the stress generates relative vorticity during the wind-forcing (Schwab & Beletsky 2003; Shimizu & Imberger 2007). This implies that the relative vorticity serves as an inhomogeneous term in the radial eigenfunction equation (Bessel's equation), modifying the eigenfunction by necessitating particular solutions in addition to the free modal (Bessel) solutions. The wind-generated vorticity (i.e. particular solution) remains even after the wind is turned off to conserve the total vorticity in the system. Recalling our definition of the forcing duration t_0 in (7.2), t_0 increases in proportion to $\mathscr{B}^{-1}$. With these issues in mind, we believe that the long-time, wind-generated relative vorticity field becomes significant compared to Kelvin or Poincaré wave modes, which can consequently render (7.10) and (7.12) invalid, since (7.10) and (7.12) are based on a simple assumption that admits only Kelvin and Poincaré wave modes in the field. We first wondered whether the ratio discrepancy for small $\mathscr{B}$ might be caused by the nonlinearity, but we discarded the possibility after we obtained nearly the same results (e.g. see figure 25*b*) by running the code for the linear hydrostatic configuration.

From (7.10), requiring the term inside the square root to be positive, we have the constraints that

$$\frac{\sigma_2}{\mu_2} < \gamma < \frac{\sigma_1}{\mu_1} \quad \text{or} \quad \frac{\sigma_1}{\mu_1} < \gamma < \frac{\sigma_2}{\mu_2}. \tag{7.13}$$

These constraints imply that the gross potential-to-kinetic energy ratio must be within a range between those of Kelvin and Poincaré waves. But, as seen in figure 25(*a*), γ is outside the range for small $\mathscr{B}$. This discrepancy most likely derives from the non-zero curl of the wind stress as discussed above.

From figure 27(*b*), the Poincaré wave energy is pronounced for larger $\mathscr{B}$ (>2), although the Kelvin wave has a larger amplitude as seen in figure 27(*a*). This is because, for large $\mathscr{B}$, the frequency of the Poincaré wave approaches -1, which causes horizontal velocities to become pronounced via the relation $(U, V) \propto (1-\omega^2)^{-1}$ as described in (3.2) and (7.3); also the Kelvin wave becomes more localized to the basin perimeter ($l_K \sim c/\mathscr{B}$). For $n_s = 1$ (parabolic stress shape), the stress is biased at the basin centre, favouring energy input in Poincaré waves over the Kelvin wave, whose energy is confined near the basin perimeter.

8. Conclusions

A weakly nonlinear weakly dispersive wind-forced variable environmental evolution model is derived for a continuously stratified circular basin. The model was numerically simulated with the vertical modes in the field restricted to include only the lowest vertical mode. We investigated first the field evolution starting from initial conditions corresponding to hydrodynamically balanced linear Kelvin and Poincaré waves in a basin of both uniform and perturbed depth. Then we investigated the wind-forced response, and evaluated our simulation results employing the linear hydrostatic model with an emphasis on energetically dominant Kelvin and Poincaré waves.

Although the linear theory gives a set of wave solutions of permanent form and speed, our simulation exhibited that those linear solutions are not preserved in the nonlinear evolution. The Kelvin wave steepens as it travels, and the steepened front generates oscillatory waves owing to a balance between weak nonlinearity and non-hydrostatic effects. Through this nonlinear effect, the field energy is transferred from basin scale to sub-basin scales. The rate of steepening is a strong function of the wave amplitude, Burger number, vertical structure, depth-to-horizontal scale ratio and typical depth within a Rossby radius along the basin perimeter. The field kinetic energy is still confined near the basin perimeter even after the development of oscillatory waves. Energy transfer from Kelvin to Poincaré wave modes is thus insignificant.

On the other hand, Poincaré wave evolution does not exhibit such a hyperbolic character as observed in Kelvin wave evolution. The amplitude of a Poincaré wave is modulated, losing its symmetry and later returning to 'near' symmetry as it evolves, exhibiting a pseudo recurrence character. The amplitude modulation is a strong function of the initial wave amplitude, and the depth at the basin centre. The energy is contained primarily in azimuthal mode one with preference for rather higher radial modes. This structure of the modal energy is persistent for longer evolution times following the initial adjustment. The field kinetic energy is offshore-biased at all times, with minor deviation from symmetry. Similar to Kelvin wave evolution, there is no significant energy transfer from the Poincaré to the Kelvin wave mode.

The aforementioned evolution trends of the Kelvin and the Poincaré waves are very similar to results presented in a recent work by de la Fuente *et al.* (2008) using a two-layer, shallow water model with weak non-hydrostatic effect in a circular lake of uniform depth. Our results are based on a rationally derived asymptotic model for arbitrary stratification in the polar coordinates, which preserves geometric symmetry, and the model simulations were carried out through a novel scheme possessing full spectral accuracy.

Uniform or near-uniform wind stress excites Kelvin and Poincaré wave modes predominantly. If the forcing is not too strong, the linear theory can still be an effective tool to estimate the initial energy resident in these dominant modes. Also, the frequency information obtained from the linear dispersion relation is quite useful to diagnose the internal wave spectrum in the frequency space. After a single wind-forcing event, the amplitude of the Kelvin wave is greater than the Poincaré counterpart. This is quite misleading, however, because the total energy of the Kelvin wave becomes much less than that of the Poincaré wave, especially for large lakes, or perhaps for lakes with weak stratification. Considering the field evolution character of these waves, energy dissipation is expected to be greatly dependent on the lake dimension and the stratification (Burger number). In large lakes for example, the shore-confined post-steepened oscillatory Kelvin waves can shoal and eventually break as they pass through three-dimensional irregular bathymetry, enhancing mixing at the shore and radiating near-buoyancy-frequency short internal waves off the shore. Poincaré waves instead can lose energy via bottom friction around the basin centre due to the large bottom current there. To estimate the gross energy dissipation rate in a basin, it is important to estimate the energy partition in these dominant modes at the starting point.

Hydrodynamic models for large lakes are usually based on the hydrostatic assumption, one that has been rationalized by noting that the horizontal length scale is much larger than the vertical scale, rendering vertical advection negligible at the leading order. However, if the horizontal field gradient becomes very large due to nonlinear steepening, vertical advection cannot remain negligible, as demonstrated by the numerical simulation presented in this study. The non-hydrostatic oscillatory waves are usually of subgrid scale in large lakes. Even a non-hydrostatic model is unable to capture the physics unless otherwise using sufficiently fine finite-difference mesh. To improve the fidelity of the hydrodynamic models, there will be a need to model the dissipation rate of such subgrid scale waves.

Our study has focused on the evolution of predominant modes in a context of weak nonlinearity with weak topography perturbation in a circular basin. This simplicity is probably why the energy exchange between these dominant modes appeared very weak. Sloping shelf and irregular perimeter are expected to greatly enhance such modal energy transfer through bathymetric gyres and strong nonlinearity. It should be added that the higher vertical modes are also expected to play an important role in nonlinear energy transfer. These are important issues deserving future study.

The authors acknowledge the receipt of helpful comments from anonymous reviewers.

REFERENCES

ANTENUCCI, J. & IMBERGER, J. 2001 Energetics of long internal gravity waves in large lakes. *Limnol. Oceanogr.* **46** (7), 1760–1773.

ANTENUCCI, J., IMBERGER, J. & SAGGIO, A. 2000 Seasonal evolution of the basin-scale internal wave field in a large stratified lake. *Limnol. Oceanogr.* **45** (7), 1621–1638.

BELETSKY, D. & O'CONNOR, W. P. 1997 Numerical simulation of internal Kelvin waves and coastal upwelling fronts. *J. Phys. Oceanogr.* **27**, 1197–1215.

BENNETT, J. R. 1973 A theory of large-amplitude Kelvin waves. *J. Phys. Oceanogr.* **3**, 57–60.

BOEGMAN, L., IVEY, G. N. & IMBERGER, J. 2005*a* The degeneration of internal waves in lakes with sloping topography. *Limnol. Oceanogr.* **50** (5), 1620–1637.

BOEGMAN, L., IVEY, G. N. & IMBERGER, J. 2005*b* The energetics of large-scale internal wave degeneration in lakes. *J. Fluid Mech.* **531**, 159–180.

BOYD, J. P. 1998 High order models for the nonlinear shallow water wave equations on the equatorial beta-plane with application to Kelvin wave frontogenesis. *Dyn. Atmos. Oceans* **28**, 69–91.

BOYD, J. P. 2001 *Chebyshev and Fourier Spectral Methods*, 2nd edn. Dover.

CSANADY, G. T. 1967 Large-scale motion in the Great Lakes. *J. Geophys. Res.* **72** (16), 4151–4162.

CSANADY, G. T. 1968 Wind-driven summer circulation in the Great Lakes. *J. Geophys. Res.* **73** (7), 2579–2589.

CSANADY, G. T. 1972 Response of large stratified lakes to wind. *J. Phys. Oceanogr.* **2** (1), 3–13.

CSANADY, G. T. 1975 Hydrodynamics of large lakes. *Annu. Rev. Fluid Mech.* **7**, 357–386.

FARMER, D. M. 1978 Observations of long nonlinear internal waves in lake. *J. Phys. Oceanogr.* **8**, 63–73.

FEDOROV, A. V. & MELVILLE, W. K. 1995 Propagation and breaking of nonlinear Kelvin waves. *J. Phys. Oceanogr.* **25**, 2518–2531.

FEDOROV, A. V. & MELVILLE, W. K. 2000 Kelvin fronts on the equatorial thermocline. *J. Phys. Oceanogr.* **30**, 1692–1705.

DE LA FUENTE, A., SHIMIZU, K., IMBERGER, J. & NIÑO, Y. 2008 The evolution of internal waves in a rotating, stratified, circular basin and the influence of weakly nonlinear and nonhydrostatic accelarations. *Limnol. Oceanogr.* **53** (6), 2738–2748.

GERKEMA, T. 2003 Development of internal solitary waves in various thermocline regimes: a multi-modal approach. *Nonlinear Process. Geophys.* **10**, 397–405.

GRIFFITHS, S. D. & GRIMSHAW, R. H. J. 2007 Internal tide generation at the continental shelf modelled using a modal decomposition: two-dimensional results. *J. Phys. Oceanogr.* **37**, 428–451.

GRIMSHAW, R. 1985 Evolution equations for weakly nonlinear, long internal waves in a rotating fluid. *Stud. Appl. Math* **73**, 1–33.

HELFRICH, K. R. 1992 Internal solitary wave breaking and run-up on a uniform slope. *J. Fluid Mech.* **243**, 133–154.

HODGES, B. R., IMBERGER, J., SAGGIO, A. & WINTERS, K. B. 2000 modelling basin-scale internal waves in a stratified lake. *Limnol. Oceanogr.* **45** (7), 1603–1620.

HORN, D. A., IMBERGER, J. & IVEY, G. N. 2001 The degeneration of large-scale interfacial gravity waves in lakes. *J. Fluid Mech.* **434**, 181–207.

HORN, D. A., IMBERGER, J., IVEY, G. N. & REDEKOPP, L. G. 2002 A weakly nonlinear model of long internal waves in closed basins. *J. Fluid Mech.* **467**, 269–287.

Hunkins, K. & Fliegel, M. 1973 Internal undular surges in Seneca Lake: a natural occurrence of solitons. *J. Geophys. Res.* **78**, 539–548.

Hüttemann, H. & Hutter, K. 2001 Boroclinic solitary waves in a two-layer fluid system with diffusive interface. *Exp. fluids* **30**, 317–326.

Lamb, Sir H. 1932 *Hydrodynamics*, 6th edn. Dover.

Matsushima, T. & Marcus, P. S. 1995 A spectral method for polar coordinates. *J. Comput. Phys.* **120**, 365–374.

Maxworthy, T. 1983 Experiments on solitary internal Kelvin waves. *J. Fluid Mech.* **129**, 365–383.

Melville, W. K., Tomasson, G. G. & Renouard, D. P. 1989 On the stability of Kelvin waves. *J. Fluid Mech.* **206**, 1–23.

Michallet, H. & Ivey, G. N. 1999 Experiments on mixing due to internal solitary waves. *J. Geophys. Res.* **104** (C6), 13467–13477.

Ripa, P. 1982 Nonlinear wave–wave interactions in a one-layer reduced-gravity model on the equatorial β-plane. *J. Phys. Oceanogr.* **12**, 97–111.

Rueda, J. R., Schladow, S. G. & Pálmarsson, S. Ó. 2003 Basin-scale internal wave dynamics during a winter cooling period in a large lake. *J. Geophys. Res.* **108** (C3), 3907.

Sakai, T. & Redekopp, L. G. 2009*a* An application of one-sided Jacobi polynomials for spectral modelling of vector fields in polar coordinates. *J. Comput. Phys.* **228**, 7069–7085.

Sakai, T. & Redekopp, L. G. 2009*b* A weakly nonlinear model for multi-modal evolution of wind-generated long internal waves in a closed basin. *Nonlinear Process. Geophys.* **16**, 487–502.

Sakai, T. & Redekopp, L. G. 2010 A parametric study of the generation and degeneration of wind-forced, long internal waves in narrow lakes. *J. Fluid Mech.* **645**, 315–344.

Schwab, D. J. & Beletsky, D. 2003 Relative effects of wind stress curl, topography, and stratification on large-scale circulation in Lake Michigan. *J. Geophys. Res.* **108** (C2), 3044.

Shimizu, K. & Imberger, J. 2007 Horizontal structure and excitation of primary motions in a strongly stratified lake. *Limnol. Oceanogr.* **52** (6), 2641–2655.

Stashchuk, N., Vlasenko, V. & Hutter, K. 2005 Numerical modelling of disintegration of basin-scale internal waves in a tank filled with stratified water. *Nonlinear Process. Geophys.* **12**, 955–964.

Stocker, R. & Imberger, J. 2003 Energy partitioning and horizontal dispersion in a stratified rotating lake. *J. Phys. Oceanogr.* **33**, 512–529.

Tomasson, G. G. & Melville, W. K. 1990 Nonlinear and dispersive effects in Kelvin waves. *Phys. Fluids* A **2** (2), 189–193.

Verkley, W. T. M. 1997 A spectral model for two-dimensional incompressible fluid flow in a circular basin. Part I. Mathematical formulation. *J. Comput. Phys.* **136**, 100–114.

Vlasenko, V. & Hutter, K. 2001 Generation of second mode solitary waves by the interaction of a first mode soliton with a sill. *Nonlinear Process. Geophys.* **8**, 223–239.

Vlasenko, V. & Hutter, K. 2002 Numerical experiments on the breaking of solitary internal waves over a slope-shelf topography. *J. Phys. Oceanogr.* **32**, 1779–1793.

Wake, G. W., Gula, J. & Ivey, G. N. 2004 Periodic forcing of baroclinic basin-scale waves in a rotating stratified basin. In *Proceedings of 15th Australasian Fluid Mechanics Conference*, The University of Sydney, Sydney, Australia.

Wake, G. W., Ivey, G. N. & Imberger, J. 2005 The temporal evolution of baroclinic basin-scale waves in a rotating circular basin. *J. Fluid Mech.* **523**, 367–392.

Wang, Y. & Hutter, K. 1998 A semi-implicit semispectral primitive equation model for lake circulation dynamics and its stability performance. *J. Comput. Phys.* **139**, 209–241.

Zabusky, N. J. & Kruskal, M. D. 1965 Interaction of “solitons” in a collisionless plasma and the recurrence of initial states. *Phys. Rev. Lett.* **15**, 240–243.